

# Investigating the influence of divertor baffles on nitrogen-seeded detachment in TCV with SOLPS-ITER simulations and TCV experiments

G. Sun,<sup>1</sup> H. Reimerdes, C. Theiler, B.P. Duval, M. Carpita, C. Colandrea, R. Ducker, O. Février, S. Gorno, L. Simons, E. Tonello, the EUROfusion tokamak exploitation team<sup>2</sup> and the TCV team<sup>3</sup>

*Ecole Polytechnique Fédérale de Lausanne (EPFL), Swiss Plasma Center (SPC), CH-1015 Lausanne, Switzerland*

Plasma edge simulations with the SOLPS-ITER code are performed to study the influence of divertor baffles on nitrogen-seeded detachment in TCV L-mode discharges. In SOLPS-ITER simulation, the nitrogen seeding with baffles is found to yield lower target temperatures and heat fluxes than with baffles-only and with seeding-only. The neutral compression increases with baffles, due to lower divertor to main chamber neutral conductance, as explained by a schematic neutral transport model with baffles. The nitrogen retention, defined as the ratio of average nitrogen nuclei density in divertor and main chamber, increases with the seeding rate if baffled, and remains constant if unbaffled. At the same separatrix plasma density, the nitrogen retention with baffles is lower than the unbaffled retention at low seeding levels and is higher at high seeding levels, which is explained by the changes of nitrogen ion and neutral transport with baffles and seeding. The baffled carbon retention is higher than the unbaffled retention due to lower divertor to main chamber carbon neutral conductance. Baffles also redistribute more impurity radiations from the main chamber region into the divertor. The predicted trends of target parameters, the distribution of radiation and neutrals are well supported by TCV experiments, though discrepancies in the absolute values remain. The simulations generally yield an overall colder and denser divertor, consistent with previous SOLPS-ITER simulations of Ohmically heated L-modes in TCV. The successful comparison of simulation and experiment, together with the understanding gained from the neutral transport model, increases the confidence in the SOLPS simulations for the next TCV divertor upgrade.

Keywords: tokamak, divertor detachment, nitrogen seeding, neutral baffling, SOLPS-ITER simulation

## 1. INTRODUCTION

The divertor targets of a fusion reactor based on the tokamak concept will be exposed to intense plasma heat fluxes. Controlling plasma-surface interactions at the targets within sustainable levels will likely require operating its divertor in the detached regime, characterized by low target plasma temperatures and reduced particle and heat fluxes [1-3]. Accessing a detached divertor requires sufficient power dissipation in the divertor volume, which is commonly achieved by operating at high plasma density and/or by seeding impurities [4-7]. Increasing divertor closure can further facilitate the access to

---

<sup>1</sup> Author to whom correspondence should be addressed: [guang-yu.sun@epfl.ch](mailto:guang-yu.sun@epfl.ch)

<sup>2</sup> See the author list of E. Joffrin et al. Nuclear Fusion 64 112019 (2024)

<sup>3</sup> See the author list of H. Reimerdes et al. Nuclear Fusion 62 042018 (2022)

detachment [8-11]. The tokamak  $\lambda$  configuration variable (TCV) [12] contributes to the development and optimization of a divertor solution for a fusion reactor through proof-of-principle experiments and plasma edge model validation.

Impurity seeding converts a portion of the scrape-off layer (SOL) heat flux into radiation, which distributes power more evenly across the vessel wall, rather than locally concentrating it onto the divertor targets. Nitrogen and noble gases (e.g. Ne, Ar, Kr) are commonly used impurity species. However, high core impurity concentration can lead to excessive confinement degradation or intolerable fuel dilution [13]. Impurities with higher charge numbers,  $Z$ , have higher radiation efficiency in the plasma core and are more prone to lead to excessive core radiation or even a discharge collapse [14-16]. Low- $Z$  impurities radiate less in the plasma core but can strongly dilute the fusion fuel, which may be intolerable in a reactor [4]. Since the radiation efficiencies of impurities are functions of the electron temperature [4, 17], the optimum choice of impurity species depends on the SOL temperature, and is, therefore, device dependent. Nitrogen seeding provides an operation window of sufficient power radiation with tolerable core confinement in medium size devices, and has been widely used in TCV experiments [18-20].

Increasing divertor closure was found to increase the confinement of neutral particles in the divertor and enhance the transfer of momentum and energy from the plasma to neutrals [21-24]. Flexible baffles have been installed in TCV during dedicated campaigns to explore the role of neutrals for plasma exhaust [25]. Too tight divertor closure can, however, lead to excessive heat fluxes and recycling on the main-plasma-facing side of the baffles [26]. The optimal location and closure of TCV baffles have been investigated in detail through both simulations and experiments [24, 26, 27].

Previous TCV simulations investigated neutral baffling without impurity seeding [28-30] and seeding without baffles [31]. The present work extends the investigations to nitrogen-seeded detachment with baffles, combining SOLPS-ITER simulations and TCV experiments, to provide an improved understanding of how baffles affect deuterium and impurity transport in a seeded discharge. Impurities are subject to thermal and friction forces, with the parallel force balance and  $E \times B$  drifts determining the impurity leakage from the divertor into the main chamber. Recent work further suggested that the relative location between the impurity stagnation point, where the impurity flow velocity near the separatrix is zero, and the impurity ionization front regulates the impurity leakage [32]. Baffles affect both locations and inevitably complicate the behavior of impurities, motivating the investigations of the interplay between baffling and seeding.

The paper is organized as follows. Section 2 introduces the adopted SOLPS-ITER simulation model. In Section 3, simulated upstream and target profiles, neutral compression, impurity and radiation distributions are analyzed in both baffled

and unbaffled conditions. A schematic neutral transport model is introduced to explain how baffles affect the neutral deuterium and impurity distribution. In Section 4, the model predictions are compared with TCV experiments. Trends identified in Section 3 are validated and the discrepancies are discussed and explained. Concluding remarks are given in Section 5.

## 2. SIMULATION MODEL

This section introduces the SOLPS-ITER simulation setup. SOLPS-ITER is a 2D transport code to simulate the plasma edge of magnetic fusion devices [33-35]. It combines the 2D multi-fluid plasma transport model B2.5 and the Monte-Carlo neutral transport kinetic model EIRENE [36], and is used to predict the divertor performance in ITER and in various reactor designs. The B2.5 model solves for the plasma parameters (density  $n$ , parallel ion velocity  $v_{i,||}$ , temperature  $T$ , potential  $\phi$ , etc.) from the balance equations of particle number, parallel momentum, energy and charge. Meanwhile, EIRENE simulates the plasma-neutral interactions and calculates the source terms of the plasma fluid equations in B2.5. The surface reflections rely on the TRIM database, the radiation is evaluated using ADAS, and reaction rates (cf. Table I) are obtained from AMJUEL, HYDHEL and METHANE. The currently adopted code version is 3.0.8.

The considered equilibrium is a TCV lower single null configuration with a plasma current of 250 kA and a magnetic field of 1.4 T, typically used in Ohmically heated L-mode density ramp and seeding experiments, Figure 1(a). The generated curvilinear quadrangular B2.5 computational grid and the triangular EIRENE mesh are shown in Figure 1(b, c). While the former only covers the scrape-off layer (SOL) up to the baffles, the latter extends to the vessel wall. The geometry of the short inner and long outer baffles (referred to as the SI-LO configuration) corresponds to the experimental setup and is the same as in previous simulations [28]. Since the plasma grid is limited by the baffle tips, the sheath boundary condition can only be applied at the target plates, whereas constant density and temperature fall-off lengths are set for far SOL boundaries. Radial plasma flow across the far SOL plasma grid boundary is returned as neutrals, which may result in an overestimation of the recycling on the main chamber vessel wall. The problem is avoided in other edge codes such as SolEdge2D [37] and efforts are underway to extend also the plasma grid in SOLPS-ITER to the wall [38, 39].

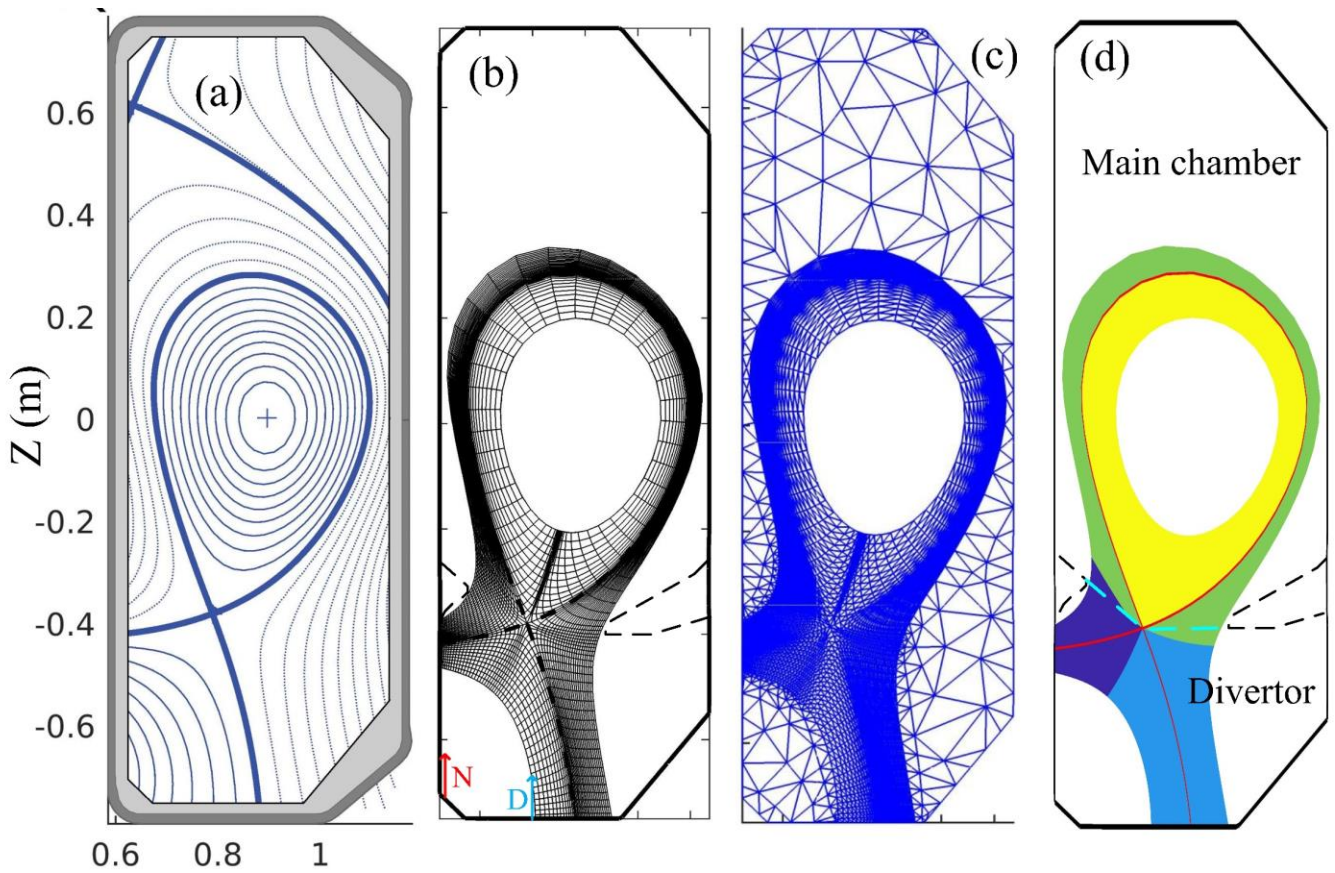


Figure 1. Employed magnetic equilibrium and generated simulation grid. (a) Equilibrium generated with LIUQE of TCV discharge 68313 at  $t=1.0$  s. (b) B2.5 grid with nitrogen and deuterium puff locations marked with arrows and optional baffles with dashed lines. (c) EIRENE grid for the unbaffled option. (d) Distinct regions of the B2.5 grid, including inner divertor (dark blue), outer divertor (light blue), upper SOL (green) and core (yellow). Main chamber and divertor regions are separated by line segments (cyan) connecting the X-point and the baffle tips.

Considered plasma species include all charge states of deuterium ( $D_2, D, D^+, D_2^+$ ), carbon ( $C - C^{6+}$ ) and nitrogen ( $N - N^{7+}$ ). Due to the short disassociation mean free path of  $N_2$ , only atomic  $N$  is considered. In addition, chemical reactions such as the formation of nitrogen hydrides and hydrocarbon are neglected. Detailed reactions are listed in Table I. Note, that recent studies highlighted a greater importance of plasma-molecule interaction, with systematic errors in some of the code-embedded reaction cross sections [40]. For the present work, the default reaction list is used, without the correction for plasma-molecule interaction. Deuterium and nitrogen are puffed in the divertor private flux region (PFR), Figure 1(b), as typically done in TCV experiments. Ions and neutral atoms colliding with the target are either recycled as thermalized molecules or reflected as fast atoms, as described by EIRENE and TRIM [41]. The recycling coefficient, defined as the ratio of recycled neutral flux and incident particle flux  $R = \Gamma^{recycled} / \Gamma^{in}$ , is set to 0.99 for deuterium and 0 for carbon. With a previous TCV study showing that a recycling coefficient of 1.0 for neutral nitrogen and 0.3-0.5 for nitrogen ions provide the best match between the

spectroscopic measurements of nitrogen emission lines and SOLPS simulation results [31], a value of 0.3 is chosen. Ion and neutral particle impact onto the wall also releases wall material (carbon here) through physical and/or chemical sputtering. The former is calculated with the Roth-Bogdansky formula [42], whereas the latter has no practical energy threshold and a value of 3.5% is chosen following previous SOLPS simulation for TCV [28]. The selected chemical sputtering yield is comparable with the TCV experiment results [43], and produces edge carbon concentration consistent with TCV spectroscopic measurements [30].

TABLE I. Reactions considered in the simulations and corresponding database.

Index	Reference code	Type	Reaction
AMJUEL			
1	H.4/H.10 2.1.5	Ionization	$D + e \rightarrow D^+ + 2e$
2	H.4/H.10 2.6A0	Ionization	$C + e \rightarrow C^+ + 2e$
3	H.4/H.10 2.7A0	Ionization	$N + e \rightarrow N^+ + 2e$
4	H4 2.2.9	Ionization	$D_2 + e \rightarrow D_2^+ + 2e$
5	H4 2.2.5g	Dissociation	$D_2 + e \rightarrow D + D + e$
6	H4 2.2.10	Ionization/dissociation	$D_2 + e \rightarrow D^+ + D + 2e$
7	H.0/H.1/H.3 0.3T	Elastic collision	$D_2 + D^+ \rightarrow D_2 + D^+$
8	H2 3.2.3	Charge exchange	$D_2 + D^+ \rightarrow D_2^+ + D$
9	H4 2.2.12	Dissociation	$D_2^+ + e \rightarrow D^+ + D + e$
10	H4 2.2.11	Ionization/dissociation	$D_2^+ + e \rightarrow D^+ + D^+ + 2e$
11	H.4/H.8 2.2.14	Dissociation/recombination	$D_2^+ + e \rightarrow D + D$
12	H.4/H.10 2.1.8	Recombination	$D^+ + e \rightarrow D$
HYDHEL			
13	H.1/H.3 3.1.8	Charge exchange	$D^+ + D \rightarrow D + D^+$
AMMONX			
14	H.2 R-H-H	Association/ionization	$D + D \rightarrow D_2^+ + e$
15	H.2 R-H-H2	Association/ionization	$D + D_2 \rightarrow D_3^+ + e$
16	H.2 R-H2-H	Association	$D + D_2 \rightarrow 3D$
17	H.2 R-H2-H2	Dissociation	$D_2 + D_2 \rightarrow D_2 + D + D$
METHAN			
18	H.1/H.3 3.2	Charge exchange	$D^+ + C \rightarrow D + C^+$
ADAS			
19	C H.4 acd96/ H.10prb96	Recombination	$C^+ + e \rightarrow C + hv$
20	N H.4 acd96/ H.10prb96	Recombination	$N^+ + e \rightarrow N + hv$

Anomalous cross field transport is approximated by constant empirical transport coefficients, with  $D_{\perp} = 0.2 \text{ m}^2 \text{ s}^{-1}$  and  $\chi_{\perp,e} = \chi_{\perp,i} = 1.0 \text{ m}^2 \text{ s}^{-1}$  as in previous simulations [28, 31, 44], providing reasonable agreement with upstream profiles measured by Thomson scattering in Ohmically heated L-mode TCV discharges, Section 4. A constant input power of 330 kW

equally shared between the electrons and ions is set as the core boundary condition. Since this work aims at a qualitative assessment of nitrogen seeding and neutral baffling, drifts are deactivated as they require smaller time steps and cause numerical instabilities. Drifts are known to cause asymmetrical particle and power distributions in the divertor [14, 16, 29, 45].

### 3. SIMULATION OF NITROGEN SEEDING IN BAFFLED AND UNBAFFLED TCV CONFIGURATIONS

In this section, SOLPS simulations are used to analyze the influence of nitrogen seeding and neutral baffling on detachment. The discussion starts with the upstream and target profiles, and then covers the behavior of neutrals and impurities.

Discharge parameters are chosen from Ohmically heated L-mode experiments that explore the transition from the conduction-limited (high-recycling) divertor regime to the detached regime. This transition typically requires the target electron temperature,  $T_{e,t}$ , to decrease below 5 eV. A decrease of the peak target electron temperature below 5 eV is, therefore, used as a proxy for the onset of detachment. While the nitrogen seeding rate is varied up to  $8 \times 10^{20}$  atom/s with and without baffles, the deuterium fueling rates are adjusted from  $2.5 \times 10^{20}$  molecules/s to  $1.5 \times 10^{21}$  molecules/s to maintain an outboard midplane separatrix density,  $n_{e,sep} = 1.5 \times 10^{19} \text{ m}^{-3}$ .

#### 3.1. Upstream and target profiles

The change of upstream and target properties including upstream and outer target temperatures, densities, target particle and heat fluxes show the effects of baffles and nitrogen seeding on detachment. Two-point model (2PM) analyses is performed to interpret the simulation results. In TCV, the outer divertor has a longer connection length and therefore, detachment is usually first achieved in the outer divertor, while the inner divertor is usually attached in the considered SN configuration.

##### 3.1.1 Observations

At constant upstream (separatrix at the outer mid-plane) density,  $n_{e,u} = 1.5 \times 10^{19} \text{ m}^{-3}$ , the target electron temperature and heat flux (including thermal, kinetic, and potential energy fluxes) decrease with both, seeding and baffling, Figure 2(a, b). The target electron density,  $n_{e,t}$ , is higher with baffles, and is insensitive to the seeding rate, Figure 2(c). The total target particle flux of all ion species is also higher with baffles, but decreases with increasing seeding rate, Figure 2(d). The contribution of impurity particle flux in the total particle flux increases from 5% to 20% from zero to maximum seeding levels. The unbaffled outer divertor detaches (maximum  $T_{e,t} < 5 \text{ eV}$ ) for seeding rates above  $5 \times 10^{20}$  atoms/s and the baffled divertor is already detached without seeding, Figure 2(a).

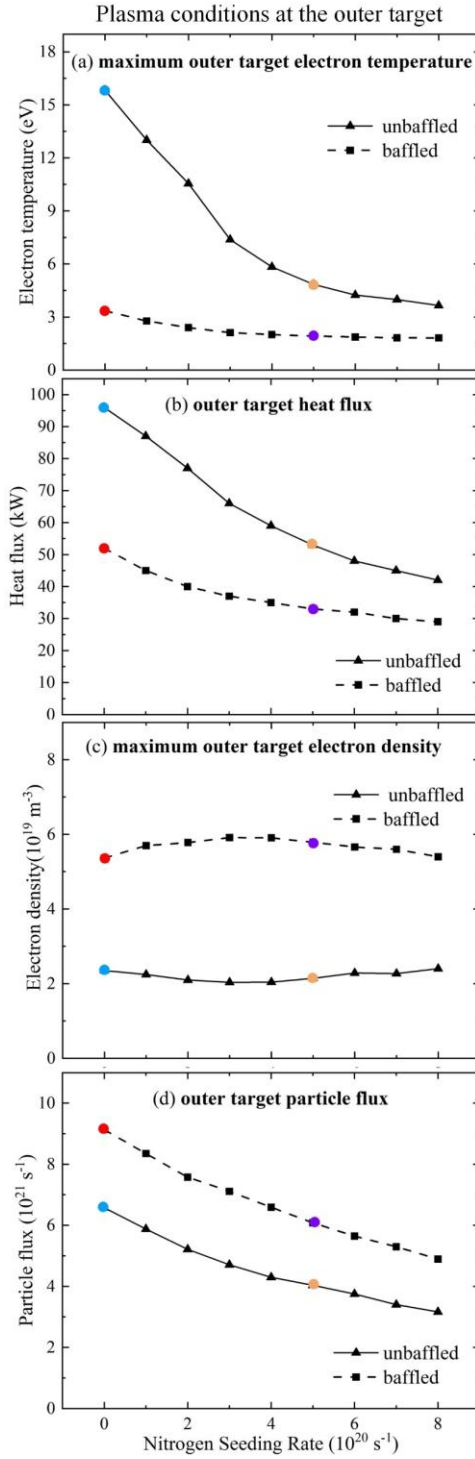


Figure 2. Dependence of (a) the outer target peak electron temperature, (b) parallel heat flux, (c) peak electron density, and (d) total parallel particle flux of all plasma species on nitrogen seeding rate at an upstream separatrix density,  $n_{e,sep} = 1.5 \times 10^{19} \text{ m}^{-3}$ . The colored points correspond to the four simulation cases highlighted in Table II.

Four simulation cases from the seeding rate scans, Figure 2, are selected and compared to further illustrate the separate effects of nitrogen seeding and baffling, as well as the combination of both, on upstream and target parameters. They consist

of an unbaffled, unseeded case (case 1), a baffled, unseeded case (case 2), an unbaffled, seeded case (case 3), and a baffled, seeded case (case 4), Table II. The unbaffled, unseeded divertor (case 1) is attached while all other cases are detached. A nitrogen seeding rate of  $5 \times 10^{20}$  atoms/s is chosen such that the unbaffled, seeded divertor (case 3) and the baffled, unseeded divertor (case 2) have approximately the same outer target heat flux, Figure 2(b), and are, therefore, similarly favorable for power exhaust at the outer divertor target. This nitrogen seeding rate is comparable with rates used in TCV seeding experiments, and leads to a  $Z_{eff}$  of 1.9 at the outboard midplane separatrix (without baffles), which is considered tolerable in a reactor scenario [46].

TABLE II. Key input and output parameters in four selected simulation cases. The color-coding of each case is kept throughout this work.

Case	Type	1	2	3	4
Baffles		No	Yes	No	Yes
N seeding rate ( $10^{20} \text{ s}^{-1}$ )	Input	0.0	0.0	5.0	5.0
D <sub>2</sub> fueling rate ( $10^{20} \text{ s}^{-1}$ )	Input	2.9	7.3	2.5	6.7
Upstream electron separatrix temperature (eV)	Output	50.6	48.1	52.4	47.6
Upstream electron separatrix density ( $10^{19} \text{ m}^{-3}$ )	Output	1.48	1.51	1.49	1.52
Outer target maximum electron temperature (eV)	Output	15.8	3.34	4.83	1.92
Outer target maximum electron density ( $10^{19} \text{ m}^{-3}$ )	Output	2.35	5.64	2.14	5.78
Outer target heat flux (kW)	Output	96	52	53	33
Inner target heat flux (kW)	Output	140	138	90	82

Baffles increase the neutral confinement in the divertor and reduce the neutral density in the main chamber, leading to a lower ionization rate inside the last-closed-flux-surface (LCFS), Figure 3(a), and, therefore, a lower cross-field particle flux. Since the simulations assume a constant diffusivity for the cross-field transport, the electron density gradient inside the LCFS decreases. The corresponding electron temperature gradient increases accordingly due to the constant power entering from the core boundary in these simulations, Figure 3(b). Meanwhile, nitrogen seeding barely affects the gradients inside the LCFS, consistent with previous SOLPS simulations of unbaffled impurity seeding [31, 47, 48]. Neither the baffles nor seeding have a significant effect on the upstream SOL profiles at constant upstream separatrix density. As a consequence, the electron pressure in the upstream SOL also remains unaffected by the simulated baffles and/or seeding rates.

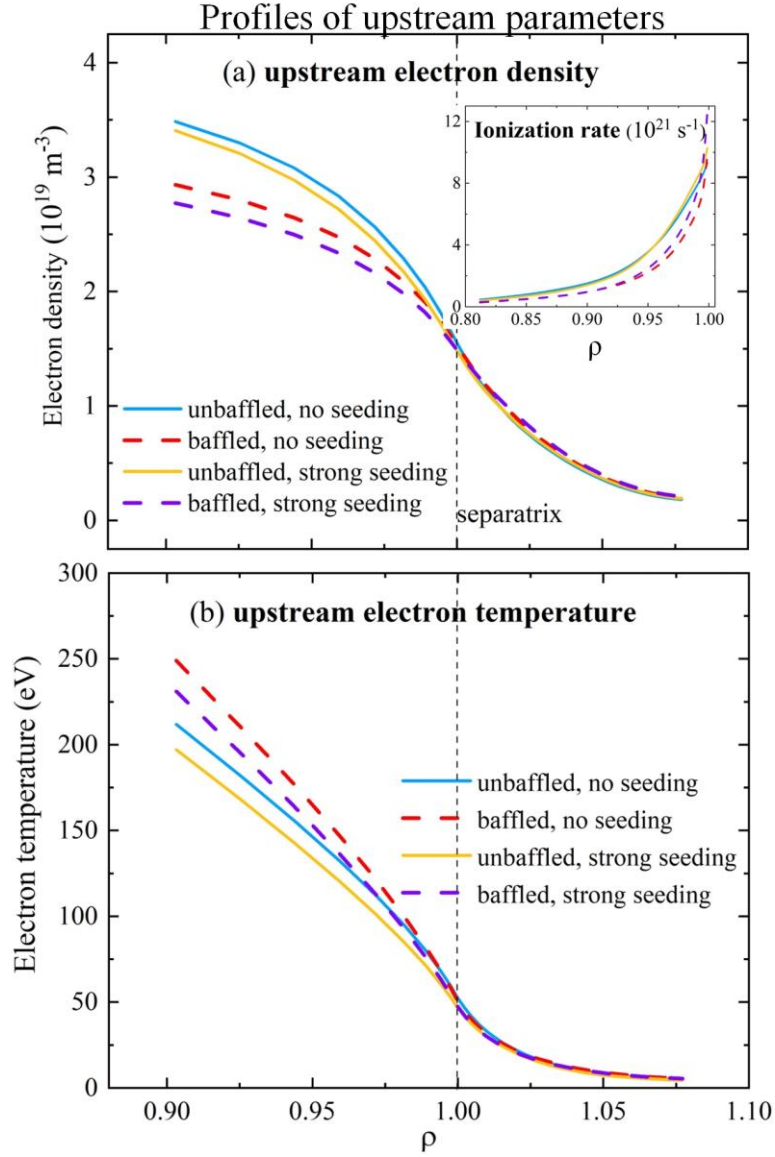


Figure 3. Upstream (a) electron density and ionization rate (insert) and (b) electron temperature profiles of the four simulation cases listed in Table II. The upstream separatrix electron density is fixed at  $1.5 \times 10^{19} \text{ m}^{-3}$  and the nitrogen seeding rate is  $5.0 \times 10^{20} \text{ s}^{-1}$  in the seeded cases.

To understand how baffles and seeding influence the access to divertor detachment, the profiles of target parameters are analyzed. Baffles increase  $n_{e,t}$  and decrease  $T_{e,t}$  across the entire target, whereas impurity seeding leaves  $n_{e,t}$  almost unchanged and primarily decreases  $T_{e,t}$ , Figure 4(a, b). The Bohm criterion at the target sheath entrance, employed as boundary condition at the divertor targets in these simulations, links  $n_{e,t}$ ,  $T_{e,t}$  and the target parallel particle flux density along magnetic field lines:

$$\Gamma_t = n_{e,t} c_{s,t} \tag{1}$$

where the sound speed  $c_{s,t} = \sqrt{(T_{e,t} + T_{i,t})/m_D}$  depends on the target electron and ion temperatures, with  $m_D$  being the main ion mass. The target parallel heat flux density along magnetic field lines including plasma thermal and kinetic energy and potential energy of ionization is approximated by:

$$q_t^{TKP} = \gamma_e T_{e,t} \Gamma_t + \gamma_i T_{i,t} \Gamma_t + \varepsilon_{pot} \Gamma_t = q_t^{TK} + \varepsilon_{pot} \Gamma_t \quad (2)$$

where  $\gamma_e$  and  $\gamma_i$  are the electron and ion sheath heat transmission coefficients and  $\varepsilon_{pot}$  is the surface recombination energy. The superscript ‘TKP’ refers to the considered thermal, kinetic and potential energy contribution and the superscript ‘TK’ indicates that the potential energy contribution is excluded. Note that heat flux contributions from radiation and neutrals are not considered. The increase of  $n_{e,t}$  with baffles is sufficiently large to counteract the decrease of  $T_{e,t}$ , resulting in a larger particle flux with baffles, Figure 4(c). Baffles result in a lower heat flux, Figure 4(d), since  $q_t^{TKP}$  has stronger dependence on  $T_{e,t}$  than the particle flux, Equation (2). Meanwhile, seeding decreases  $T_{e,t}$  whilst not significantly affecting  $n_{e,t}$ , resulting in a lower particle and heat flux. A combination of baffling and seeding results in the lowest target temperatures, Figure 4(a), the lowest target heat flux, Figure 4 (d), and an intermediate particle flux, Figure 4(c), consistent with the cumulative effects of baffling and seeding. Though baffling-only (case 2) and seeding-only (case 3) have similar  $q_t$  profile, the former features a larger  $T_{e,t}$  reduction while the latter achieves heat flux reduction by decreasing  $\Gamma_t$  in addition to a lesser  $T_{e,t}$  decrease.

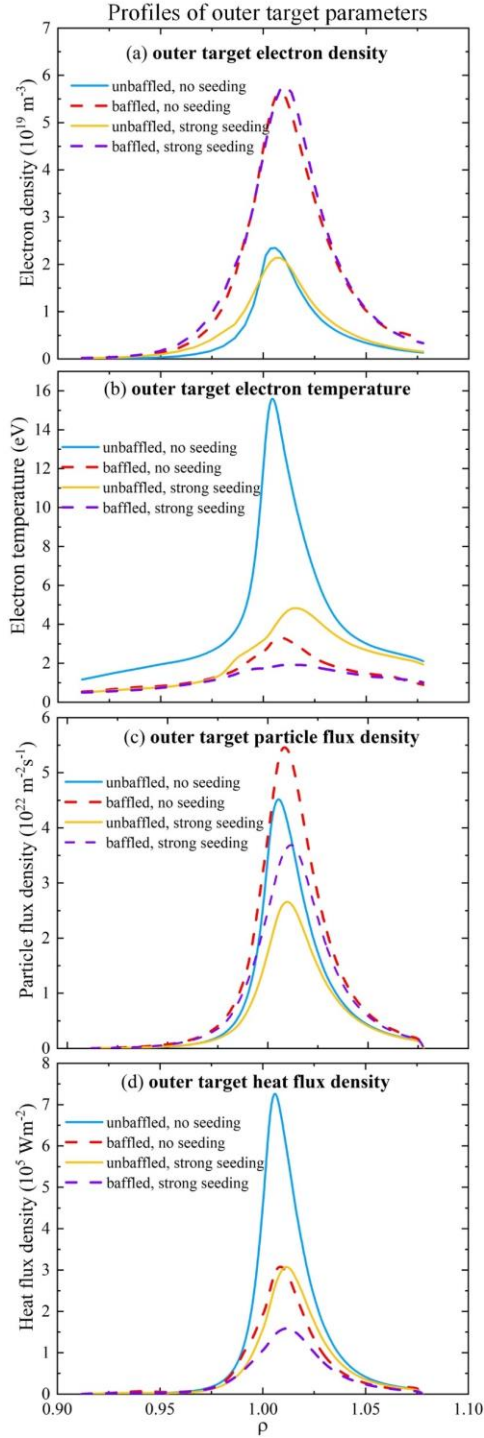


Figure 4. Outer target (a) electron density, (b) electron temperature, (c) parallel particle flux density of deuterium and (d) parallel heat flux density ( $q_t^{TKP}$ ) profiles of the four simulation cases in Table II. The upstream separatrix electron density is fixed at  $1.5 \times 10^{19} \text{ m}^{-3}$  and the nitrogen seeding rate is  $5.0 \times 10^{20} \text{ s}^{-1}$  in the seeded cases.

### 3.1.2. Two-point model analyses

The changes of target parameters with baffles and seeding are interpreted through two-point model. According to the modified 2PM model, the target density, temperature and parallel particle flux density are [1]:

$$T_{e,t}^{2PM} = \frac{8m_D q_u^{TK2}}{e\gamma^2 p_{u,tot}^2} \left(\frac{R_u}{R_t}\right)^2 \frac{(1-f_{cooling})^2}{(1-f_{mom,loss})^2} \quad (3)$$

$$n_{e,t}^{2PM} = \frac{\gamma^2 p_{u,tot}^3}{32m_D q_u^{TK2}} \left(\frac{R_t}{R_u}\right)^2 \frac{(1-f_{mom,loss})^3}{(1-f_{cooling})^2} \quad (4)$$

$$\Gamma_t^{2PM} = \frac{\gamma p_{u,tot}^2}{8m_D q_u^{TK}} \left(\frac{R_t}{R_u}\right) \frac{(1-f_{mom,loss})^2}{(1-f_{cooling})^1} \quad (5)$$

Here  $\gamma = \gamma_e + \gamma_i T_i / T_e$  is the sheath heat transmission coefficient,  $q_u^{TK}$  is the upstream parallel heat flux considering thermal and kinetic energy contribution,  $p_{u,tot}$  is the total upstream pressure, and  $R_t / R_u$  is the change in radius from upstream to target.

The two volumetric loss terms  $f_{mom,loss}$  and  $f_{cooling}$  represent the fraction of momentum and power loss, defined as:

$$f_{mom,loss} \equiv 1 - \frac{p_{t,tot}}{p_{u,tot}} \quad (6)$$

$$f_{cooling} \equiv 1 - \frac{q_t^{TK} R_t}{q_u^{TK} R_u} \quad (7)$$

Here  $p_{t,tot}$  and  $q_t^{TK}$  are the target total pressure and parallel heat flux density considering thermal and kinetic energy contribution, respectively. Since  $q_u^{TK}$  and  $p_{u,tot}$  are similar in all four cases, baffles and seeding primarily affect target parameters by changing the two loss fraction terms. Note that the decrease of target thermal and kinetic heat flux depends solely on the increase of  $f_{cooling}$ , whereas target temperature, density and particle flux are affected by both,  $f_{mom,loss}$  and  $f_{cooling}$ .

The volumetric loss terms are calculated from the simulations and used to interpret the target parameters. Baffles and nitrogen seeding, both, increase  $f_{cooling}$ , Figure 5(a). Note that the greater increase of  $f_{cooling}$  with baffling (case 2) than with seeding (case 3) is a consequence of the choice of the seeding rate in case 3 to approximately match  $q_t^{TKP}$  of case 2 (whereas the potential energy flux is not considered here). Baffles increase  $f_{mom,loss}$ , similar to  $f_{cooling}$ . Seeding only increases  $f_{mom,loss}$  near the separatrix where both upstream and target pressures, but not in the far SOL, Figure 5(b). Note that the change of  $f_{cooling}$  and  $f_{mom,loss}$  with baffles in the far SOL are less important, where the values of target parameters are much lower than near the separatrix.

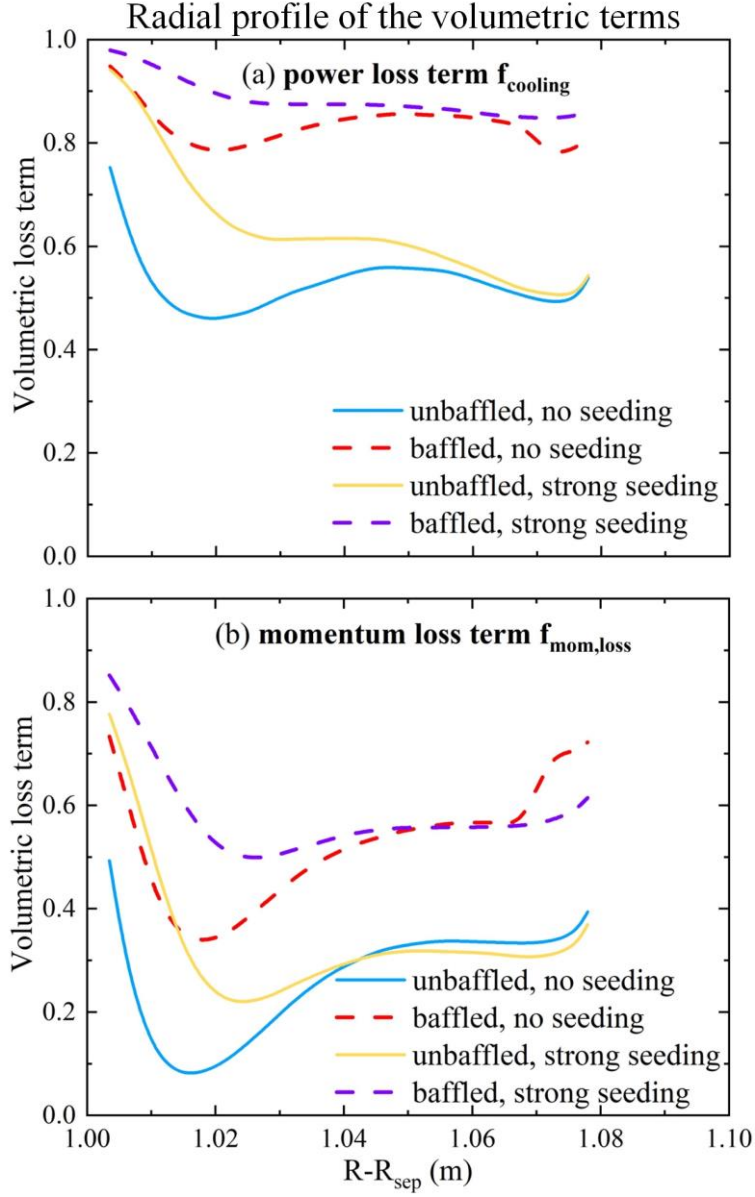


Figure 5. The volumetric power (a) and momentum (b) loss terms of the four cases in Table II. The upstream separatrix electron density is fixed at  $1.5 \times 10^{19} \text{ m}^{-3}$  and the nitrogen seeding rate set to  $5.0 \times 10^{20} \text{ s}^{-1}$  in the seeded cases.

Adding the baffles leads to a larger decrease of  $1 - f_{cooling}$  than  $1 - f_{mom,loss}$ , which explains a lower  $T_{et}$ , and a higher  $n_{et}$  and  $\Gamma_t$ . Increasing the seeding rate causes the factor  $\frac{(1-f_{cooling})^2}{(1-f_{mom,loss})^2}$  to decrease, which explains a lower  $T_{et}$ . The factor  $\frac{(1-f_{mom,loss})^3}{(1-f_{cooling})^2}$  varies little with the seeding rate, which is consistent with an  $n_{et}$  that is insensitive to the seeding rate. The target particle flux  $\Gamma_t \propto n_{et} \sqrt{T_{et}}$  consequently decreases with seeding.

## 3.2. Neutral transport

The volumetric losses, described by  $f_{cooling}$  and  $f_{mom,loss}$  in Section 3.1, are governed by the divertor neutral and impurity distributions through plasma-neutral interaction and impurity radiation. In this section, the effects of TCV gas baffles and nitrogen seeding on neutral properties are investigated by SOLPS-ITER simulation, and a schematic neutral transport model is used to interpret the simulation results. Quantities including the neutral density, neutral compression, and ionization front are analyzed, and the influences of baffles and seeding on these quantities are revealed. The TCV gas baffles are located at  $z \approx -0.35$  m, which separate the TCV vessel into the divertor region and the main chamber region. The two regions are separated by line segments connecting the two baffle tips with the X-point, Figure 1(d). The plasma region (colored areas in Figure 1(d)) is excluded when calculating the average main chamber and divertor neutral densities. The total deuterium density is defined as  $n_n \equiv 2n_{D_2} + n_D$ .

### 3.2.1 Observations

The averaged divertor neutral density,  $\langle n_n \rangle_{div}$ , significantly increases with baffles, and increases with higher nitrogen seeding rate, Figure 6(a). Without seeding, the baffled  $\langle n_n \rangle_{div}$  is 2.6 times the unbaffled  $\langle n_n \rangle_{div}$ , and their difference increases at higher seeding levels, as the increase of  $\langle n_n \rangle_{div}$  with the nitrogen seeding rate is more obvious with baffles. The averaged main chamber neutral density,  $\langle n_n \rangle_{main}$ , greatly decreases with baffles, but does not depend on the nitrogen seeding rate, Figure 6(b). Baffled  $\langle n_n \rangle_{main}$  is approximately one third of the unbaffled  $\langle n_n \rangle_{main}$  at all nitrogen seeding levels.

The neutral compression  $c_D$ , here defined as the ratio of divertor and main chamber neutral density,  $c_D = \langle n_n \rangle_{div} / \langle n_n \rangle_{main}$ , is widely used in previous works studying the divertor neutral transport [28, 49, 50]. Higher  $c_D$  indicates better divertor neutral confinement, which is one of the main motivations of increasing the divertor closure.  $c_D$  increases by a factor of seven with baffles when no nitrogen is seeded, and further increases at higher seeding levels, due to higher baffled  $\langle n_n \rangle_{div}$ , Figure 6(c).

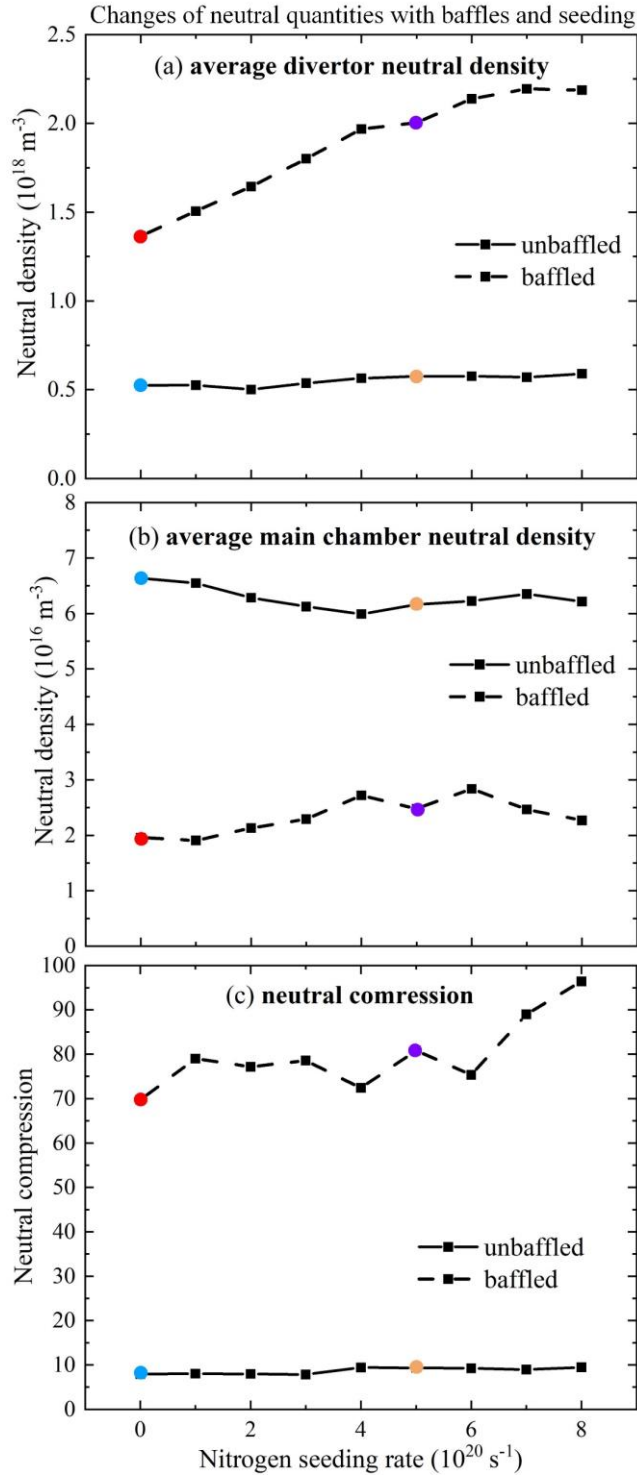


Figure 6. Nitrogen seeding scans of the averaged neutral densities and the compression. (a) Divertor neutral density. (b) Main chamber neutral density. (c) Neutral compression. The electron density at the separatrix is fixed as  $1.5 \times 10^{19} \text{ m}^{-3}$ . The colored points correspond to the four simulation cases in Table II.

The neutral distribution of the four simulation cases introduced in section 3.1 is analyzed to reveal more details of the neutral transport with baffles and seeding, Figure 7. Most divertor neutrals are located in the reservoirs of the divertor private

flux region and common flux regions (CFR), which are separated by the plasmas of the divertor legs with comparable neutral density. Neutral density decreases from the divertor CFR to the main chamber for both baffled and unbaffled divertors. Such density gradient causes the neutrals in the divertor CFR to flow upwards, which is mitigated by the baffles as CFR neutrals must penetrate the SOL plasmas near the baffle tips before reaching the main chamber region. Nitrogen seeding increases the divertor neutral density in the baffled configuration and to a lesser degree the main chamber neutral density, whereas in the unbaffled configuration, the influences of seeding on the neutral density distribution are not obvious.

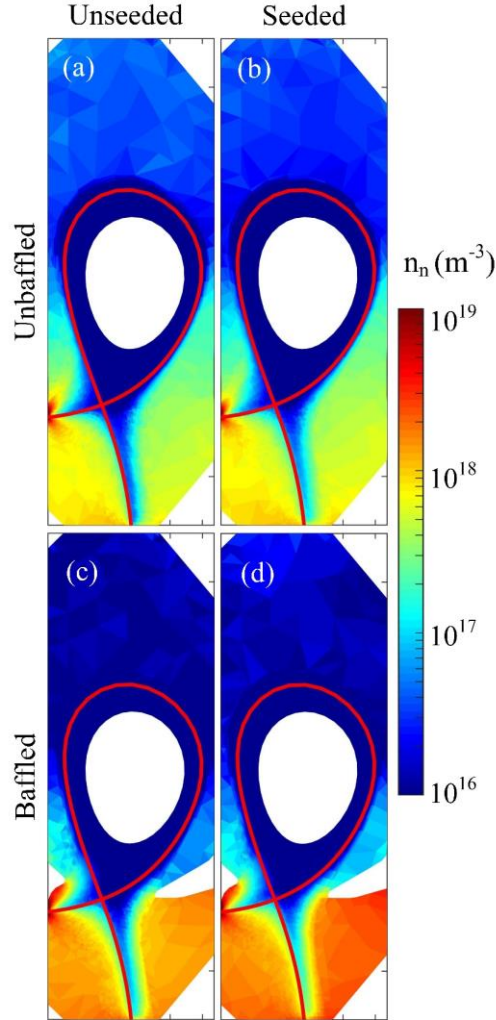


Figure 7. Total neutral density distribution,  $n_n$ , of the four cases in Table II. (a) Unbaffled, unseeded. (b) Unbaffled, seeded. (c) Baffled, unseeded. (d) Baffled, seeded. The electron density at the upstream separatrix is  $1.5 \times 10^{19} \text{ m}^{-3}$  and the nitrogen seeding rate is  $5.0 \times 10^{20} \text{ s}^{-1}$  in the seeded cases.

The changes of the neutral density distribution and plasma parameters with baffles and seeding also affect the neutral ionization distribution. Baffles increase the ionization rate in the divertor, and extend the ionization region from the targets

towards the X-point, Figure 8(a-d). Meanwhile, nitrogen seeding decreases the divertor ionization rate, and moves the ionization region away from the target, Figure 8(a-d).

The ionization front is introduced to quantitatively evaluate the changes of the ionization distribution, defined as the poloidal position above which more than 90% of the ionizations are included. Without baffles and seeding, the ionization front is located at the target as the divertor is attached. Baffles and seeding, both, move the ionization front away from the target, Figure 8(e).

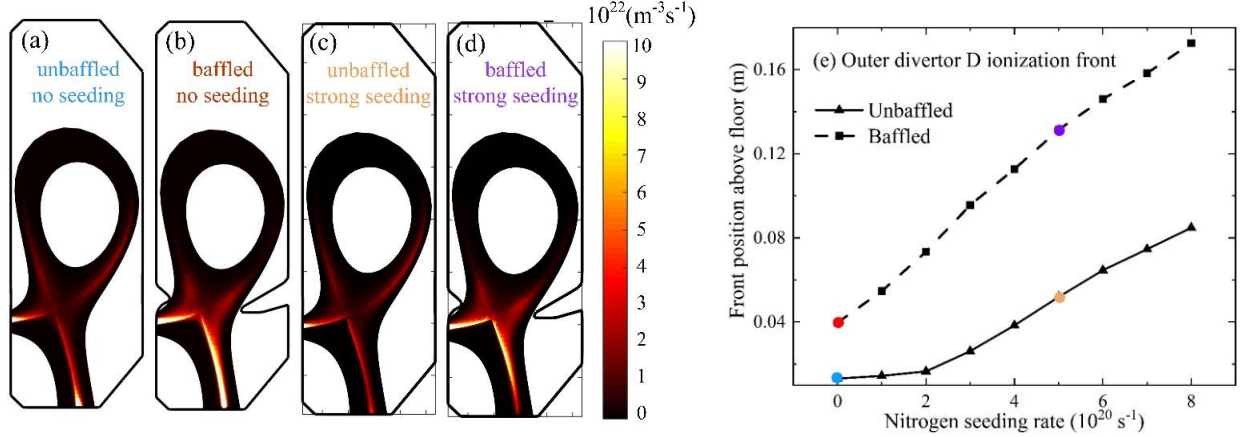


Figure 8. (a)-(d) Ionization rate distribution of the four simulation cases in Table II. The electron density at the upstream separatrix is  $1.5 \times 10^{19} \text{ m}^{-3}$  and the nitrogen seeding rate is  $5.0 \times 10^{20} \text{ s}^{-1}$  in the seeded cases. (e) Nitrogen seeding scan of the distance of the deuterium ionization front from the outer target. The colored points correspond to the four simulation cases in Table II.

### 3.2.2 Schematic model for neutral transport in a baffled divertor

The observed dependencies of neutral and ionization distributions on baffles and seeding, section 3.2.1, are explained using a simple, schematic neutral transport model [51].

The model assumes a steady-state condition, with perfect recycling, and no volumetric sources and sinks for neutrals. The neutral source from target recycling due to target ion flux,  $\Phi_{i,t}$ , are either directly ionized in front of the target,  $S_{ion,t}$ , or leak into the divertor. Divertor neutrals can either ionize in the divertor,  $S_{ion,div}$ , or transit past the baffles into the main chamber region, where they ultimately also ionize,  $S_{ion,main}$ , as illustrated in Figure 9(a). The target ion flux consists of three parts:

$$\Phi_{i,t} = S_{ion,t} + S_{ion,div} + S_{ion,main} \quad (8)$$

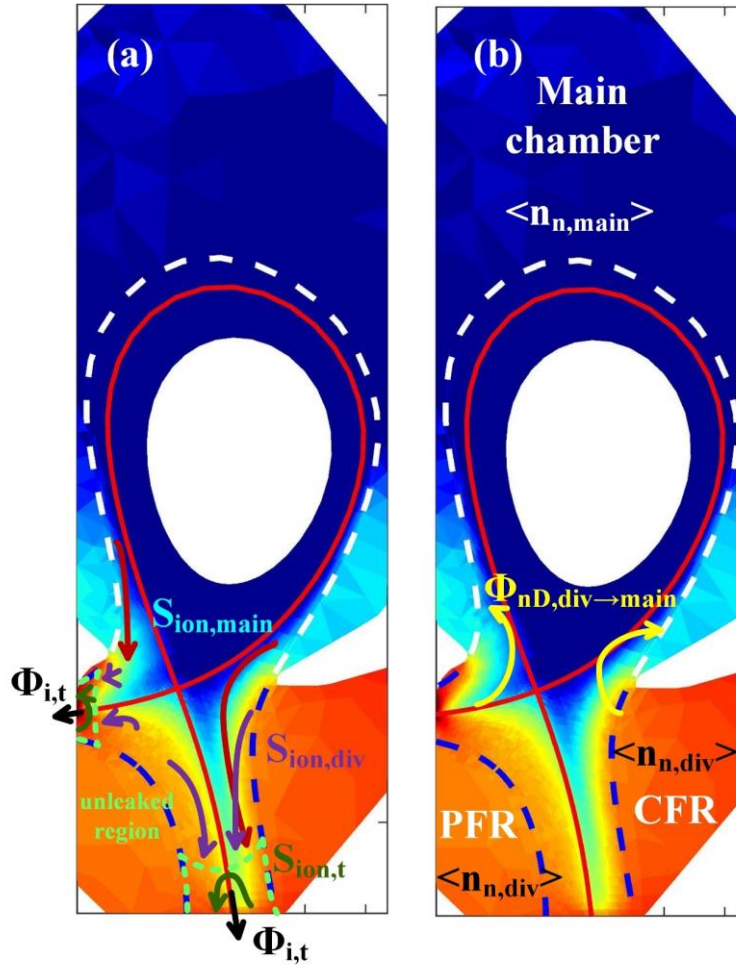


Figure 9. Schematic of the neutral transport model. (a) Three components of the target ion flux consisting of ionized divertor neutrals ( $S_{ion,div}$ ), ionized main chamber neutrals ( $S_{ion,main}$ ), and neutrals ionized near the target ( $S_{ion,t}$ ) according to Equation (8). (b) Neutral density in the divertor region  $\langle n_n \rangle_{div}$ , main chamber region  $\langle n_n \rangle_{main}$ , and neutral flux towards the main chamber region  $\Phi_{n,div \rightarrow main}$ .

Note that the last two terms on the RHS of Equation (8) represent neutrals that do not ionize directly in front of the target (i.e. the region marked in green in Figure 9(a)) and leak into the divertor, and potentially, the main chamber. They can be characterized by a leakage factor  $f_{leak}$ , which depends on the target plasma parameters and the local geometry. Equation (8) is rewritten with  $f_{leak}$  as follows:

$$\Phi_{i,t} = S_{ion,t} + f_{leak} \Phi_{i,t} \quad (9)$$

In this model, the ionization particle sinks in the divertor and main chamber are assumed to be proportional to the respective neutral densities. The neutral sink due to ionization by plasma can be characterized by an effective neutral pumping speed, with the divertor and main chamber plasma pumping speeds  $S_{div}$  and  $S_{main}$ :

$$S_{ion,div} = \langle n_n \rangle_{div} S_{div} \quad (10)$$

$$S_{ion,main} = \langle n_n \rangle_{main} S_{main} \quad (11)$$

The neutral flux from the divertor to the main chamber is proportional to the neutral density difference between the two regions and can therefore be characterized by a neutral conductance from divertor to main chamber,  $C_{cond}$ :

$$\Phi_{n,div \rightarrow main} = C_{cond} (\langle n_n \rangle_{div} - \langle n_n \rangle_{main}) \quad (12)$$

The neutral flux is marked out in Figure 9(b). Assuming  $\langle n_n \rangle_{div} \gg \langle n_n \rangle_{main}$  and that the neutral flux,  $\Phi_{n,div \rightarrow main}$ , is returned as an ion flux,  $S_{ion,main}$ , Equations (11) and (12) yield an expression for the neutral compression:

$$c_D = \frac{S_{main}}{C_{cond}} \quad (13)$$

Equation (13) indicates that  $c_D$  is inversely proportional to the neutral conductance from the divertor to the main chamber region. The model, thereby, explains the increase of  $c_D$  with baffling. Combining Equations (8)-(12), and again assuming  $\langle n_n \rangle_{div} \gg \langle n_n \rangle_{main}$  in Equation (12), in yields the corresponding divertor neutral density:

$$\langle n_n \rangle_{div} = \frac{f_{leak} \Phi_{i,tar}}{S_{div} + C_{cond}} \quad (14)$$

Equation (14) shows that the divertor neutral pressure increases with baffles, i.e. decreasing neutral conductance from divertor into the main chamber,  $C_{cond}$ . This increase will, however, saturate once  $C_{cond}$  is small compared to  $S_{div}$ .

The factors  $f_{leak}$ ,  $S_{div}$ , and  $C_{cond}$  and their dependence on baffles and seeding can be calculated from the SOLPS-ITER simulations, as discussed in the following. The calculations of these quantities are based on first-principle physical quantities from the simulations, such as the ionization distribution, neutral flux and neutral density.

The procedure of the outer divertor leakage factor calculation is briefly presented below. For a given position at the outer target,  $p_t$ , the scan of recycled neutral trajectories with emission angle  $\theta$  ranging between 0 and  $\pi$  is performed. For each neutral trajectory,  $s$ , the ratio of the differential neutral trajectory,  $ds$ , and the deuterium neutral ionization mean free path,  $\lambda_{Di}$ , is integrated between the emission location and the trajectory's intersection with the outmost plasma grid, from which  $f_{leak}$  of this neutral trajectory is calculated as follows.

$$f_{leak}(p_t, \theta) = \exp \left( - \int_{s_{start}}^{s_{end}} \frac{ds}{\lambda_{Di}(p_t, \theta)} \right) \quad (15)$$

Note that for trajectories that cross the core boundary,  $f_{leak}$  is assumed to be zero, i.e. all neutrals ionize. Charge exchange collisions are currently neglected. To calculate the total leakage factor,  $f_{leak}(p, \theta)$  is first averaged over the neutral emission angle range, where a cosine distribution is assumed, and then averaged over the extent of the target, while weighted with the target deuterium ion flux:

$$f_{leak} = \frac{1}{\Phi_{i,t}} \int_{t_{start}}^{t_{end}} \int_0^\pi \Gamma_t(p) f_{leak}(p, \theta) \frac{\cos(0.5\pi - \theta)}{2} d\theta dA(p) \quad (16)$$

Here  $\Gamma_t$  is the target ion flux density,  $\Phi_{i,t}$  is the total target ion flux,  $dA$  is the differential surface area on the target.

The divertor plasma pumping speed,  $S_{div}$ , is calculated from Equation (10), using the divertor ionization rate and the neutral density from SOLPS-ITER. The neutral conductance from the divertor to the main chamber,  $C_{cond}$ , is calculated from Equation (12), using the neutral flux crossing the interface between the divertor and the main chamber,  $\langle n_n \rangle_{div}$  and  $\langle n_n \rangle_{main}$ .

The simulations show that baffles decrease  $C_{cond}$  by almost a factor of 3, Figure 10(a). This large decrease is primarily caused by the reduction of the area that neutrals have to transit from the divertor past the baffles to the main chamber. They also reveal a slight decrease of  $C_{cond}$  with increasing seeding rate, presumably due to cooler and, hence slower, divertor neutrals, an effect that likely contributes to the reduction of  $C_{cond}$  with baffles, too. The divertor plasma pumping speed,  $S_{div}$ , also decreases with baffles by approximately 50% at all seeding levels, Figure 10(b).  $S_{div}$  also decreases with increasing seeding rate. The decrease of  $S_{div}$  with baffles and seeding could be caused by lower divertor plasma temperatures increasing the mean free path for ionization as well as by cooler divertor neutrals with baffles and seeding. The calculated leakage factor increases with both baffles and seeding, Figure 10(c). Without seeding,  $f_{leak}$  with baffles is twice as high than without baffles.  $f_{leak}$  increases faster without baffles than with baffles, leading to less of a difference at high seedings rates, Figure 10(c).

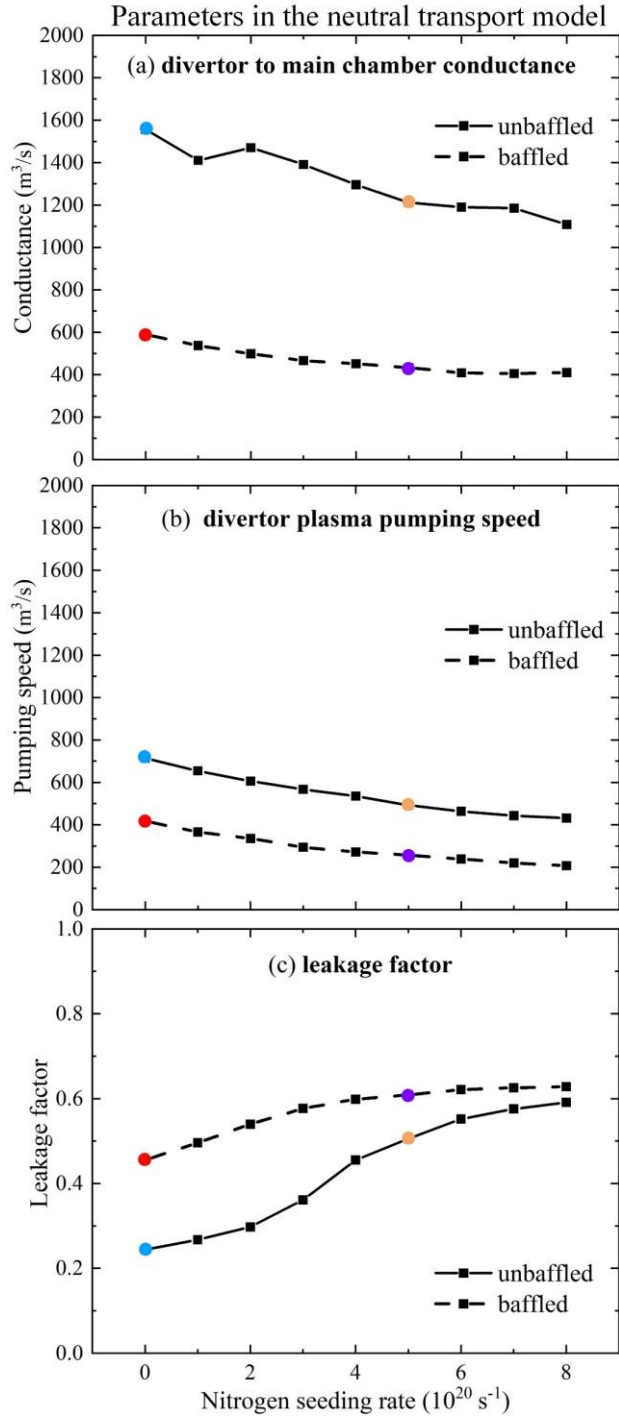


Figure 10. Nitrogen seeding scans of the factors in the neutral transport model. (a) Divertor to main chamber neutral conductance  $C_{cond}$ . (b) Divertor plasma pumping speed  $S_{div}$ . (c) Leakage factor  $f_{leak}$ . The electron density at the separatrix is fixed as  $1.5 \times 10^{19} \text{ m}^{-3}$ . The colored points correspond to the four simulation cases in Table II.

The influences of baffles and seeding on  $\langle n_n \rangle_{div}$ ,  $\langle n_n \rangle_{main}$ ,  $c_D$ , and the ionization front observed in section 3.2.1 are explained as follows based on the proposed neutral transport model. The increase of  $\langle n_n \rangle_{div}$  with baffles is primarily due to

the lower  $C_{cond}$ . Consequently, the divertor plasma becomes denser and colder, due to higher plasma-neutral collisionality. This leads to higher  $f_{leak}$  as the ionization front moves away from the target, higher target ion flux (Figure 2(d)), and lower  $S_{div}$  due to colder divertor neutrals. Baffles decrease  $\langle n_n \rangle_{main}$  because the increase of  $\langle n_n \rangle_{div}$  is less than the increase of  $\Phi_{n,div \rightarrow main}/C_{cond}$  (not shown). Higher  $\langle n_n \rangle_{div}$  and lower  $\langle n_n \rangle_{main}$  with baffles together increase  $c_D$ . Contrary to the baffles, nitrogen seeding does not considerably affect the neutral conductance, but cools down the divertor plasmas with stronger impurity radiation, which increases  $f_{leak}$ , and therefore increases  $\langle n_n \rangle_{div}$ .

It is worth pointing out that the term  $S_{div}$  is of the same order of magnitude with  $C_{cond}$  for baffled and unbaffled divertor, whereas the ratio  $C_{cond}/S_{div}$  is lower with baffles, Figure 10(a-b). With tighter baffling, it is possible that  $C_{cond} \ll S_{div}$ , such that further increase of the divertor closure can no longer increase  $\langle n_n \rangle_{div}$ . The trend that  $c_D$  increases with lower  $C_{cond}$  is unaffected with tighter baffling, according to Equation (13), where further increase of  $c_D$  by tighter baffling is likely contributed by lower  $\langle n_n \rangle_{main}$ , instead of higher  $\langle n_n \rangle_{div}$ .

### 3.3. Impurity retention and radiation

Baffles decrease the impurity neutral conductance from the divertor to the main chamber, similar to their effect on deuterium neutrals. Baffles also change the divertor  $D^+$  flow pattern, and therefore, the impurity friction force between impurities and  $D^+$ . In addition, baffles increase the target particle flux and hence the source of sputtered carbon. Consequently, the distributions of impurity neutral density, ion density, and radiated power, change with baffles. These effects are analyzed in the following, to validate the compatibility of baffles with nitrogen seeding, and their potential synergies on achieving divertor detachment.

Since both impurity neutrals and ions radiate, their total nuclei densities are studied below. The notion of *impurity retention* is introduced as the ratio of average total impurity density in the divertor and in the main chamber region:

$$R_{imp} = \frac{\langle n_{imp} \rangle_{div}}{\langle n_{imp} \rangle_{main}} \quad (17)$$

with  $n_{imp}$  the total impurity density (including neutral impurities and all ionized states), where the index *imp* is either *C* or *N* for carbon or nitrogen, respectively. The separation of the main chamber and divertor region is the same for the neutral compression. The impurity retention in the divertor varies with baffling, the impurity species, and the nitrogen seeding rate.

### 3.3.1. Analysis of nitrogen retention

Since the nitrogen recycling coefficient is well below one, wall-pumped nitrogen is replaced with a continuous nitrogen flow from a seeding valve, which is here located in the PFR of the divertor. Most seeded neutral nitrogen must, therefore, first transit through the divertor legs into the CFR, before it can be transported between the baffles into the main chamber. This leads to a considerable neutral nitrogen density difference between the PFR, the divertor CFR, and the main chamber, i.e.  $\langle n_{n,N} \rangle_{div,PFR} \gg \langle n_{n,N} \rangle_{div,CFR} \gg \langle n_{n,N} \rangle_{main}$ , Figure 11 and Figure 12(a-c). Baffles considerably increase  $\langle n_{n,N} \rangle_{div,CFR}$ , Figure 12(b), via two mechanisms. First, the divertor to main chamber neutral nitrogen conductance,  $C_{cond,N}$ , decreases with baffles, similar to neutral deuterium. Second, baffles cool down the divertor plasma, increasing the transparency of the divertor legs for neutral nitrogen and facilitating the neutral nitrogen transport from the divertor PFR to the CFR. The divertor plasma transparency also increases with seeding, causing  $\langle n_{n,N} \rangle_{div,CFR}$  to increase faster than linearly with the seeding. The increased neutral nitrogen flux from the PFR into the CFR is, however, too small to affect  $\langle n_{n,N} \rangle_{div,PFR}$ . As a result,  $\langle n_{n,N} \rangle_{div,PFR}$  is predominantly determined by the balance of seeding source in divertor PFR and the ionization of PFR neutral, and, therefore, unaffected by baffles, increasing linearly with seeding. Despite the higher value of  $\langle n_{n,N} \rangle_{div,CFR}$ , baffles decrease  $\langle n_{n,N} \rangle_{main}$  due to the lower  $C_{cond,N}$ , Figure 12(a, c).

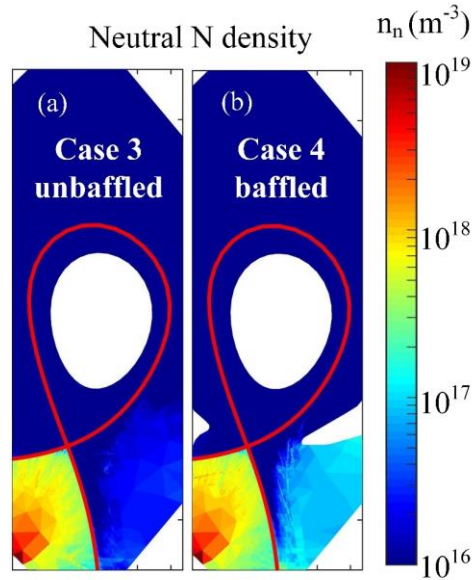


Figure 11. Neutral nitrogen distribution without and with baffles and with seeding (case 3 and 4 of Table II). (a) Neutral nitrogen density without baffles. (b) Neutral nitrogen density with baffles. The electron density at the upstream separatrix is  $1.5 \times 10^{19} \text{ m}^{-3}$  and the nitrogen seeding rate is  $5 \times 10^{20} \text{ s}^{-1}$  in the seeded cases.

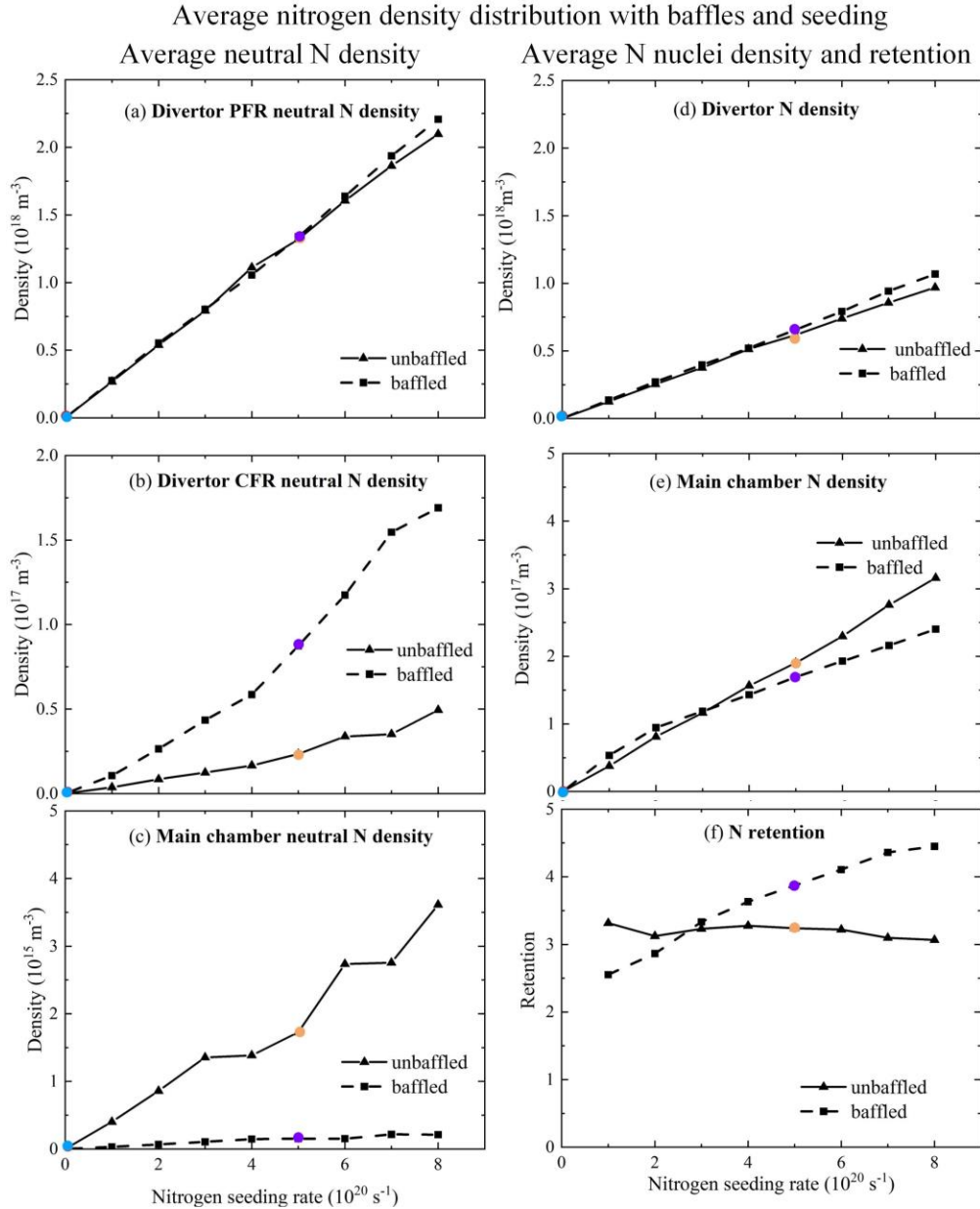


Figure 12. Average neutral nitrogen density in (a) Divertor PFR. (b) Divertor CFR. (c) Main chamber. Average nitrogen nuclei density in (d) Divertor. (e) Main chamber. The nitrogen retention (f). The electron density at upstream separatrix is fixed as  $1.5 \times 10^{19} \text{ m}^{-3}$  and the colored points correspond to the four simulation cases in Table II.

The nitrogen nuclei density, and the nitrogen retention, are affected by both nitrogen neutral and nitrogen ion densities.

Divertor neutral nitrogen, mostly from the divertor PFR neutral, contributes more than 50% to  $\langle n_N \rangle_{div}$ . Like  $\langle n_{n,N} \rangle_{div,PFR}$ ,  $\langle n_N \rangle_{div}$  increase linearly with the seeding rate, and is barely affected by baffles, Figure 12(a, d).

Meanwhile, neutral nitrogen contributes less than 1% to  $\langle n_{n,N} \rangle_{main}$  at all seeding levels in both, unbauffed and baffled divertors. Therefore, the observed trends of  $\langle n_N \rangle_{main}$  are due to a change of nitrogen ion leakage flux from divertor to the main

chamber. At low seeding rates  $\langle n_N \rangle_{main}$  increases faster with the seeding rate with baffles, Figure 12(e). This increase of nitrogen ion leakage flux in the presence of the baffles must be due to a change of the  $D^+$  flow pattern, which moves the ion stagnation point closer to the target (not shown) and, thereby, promotes nitrogen ion leakage into the main chamber. As the seeding rate increases, the dependence of  $\langle n_N \rangle_{main}$  on seeding weakens with baffles. Since these divertor plasmas feature the lowest temperatures, it may be the decrease of the ion thermal force that decreases the ion leakage and slows the increase of  $\langle n_N \rangle_{main}$  with the seeding rate.

These dependencies of  $\langle n_N \rangle_{div}$  and  $\langle n_N \rangle_{main}$  lead to a slightly lower  $R_N$  with baffle at low seeding levels, but a 47% higher  $R_N$  with baffles than without baffles at highest seeding levels, Figure 12(f).

### 3.3.2. Analysis of the carbon retention

Carbon is mainly sourced by sputtering at the target, with C leaking into, both, PFR and CFR. The neutral carbon density, therefore, exhibits smaller difference between the divertor PFR and CFR than neutral nitrogen, similar to neutral deuterium, i.e.  $\langle n_{n,C} \rangle_{div,PFR} \sim \langle n_{n,C} \rangle_{div,CFR}$ , Figure 13, Figure 14(a-c). Baffles decrease the divertor to main chamber carbon neutral conductance,  $C_{cond,C}$ , and increase the target particle flux, both leading to higher  $\langle n_{n,C} \rangle_{div,PFR}$  and  $\langle n_{n,C} \rangle_{div,CFR}$ . Seeding decreases the target particle flux, therefore slightly decreases  $\langle n_{n,C} \rangle_{div,PFR}$  and  $\langle n_{n,C} \rangle_{div,CFR}$ , Figure 14(a, b). Baffles decrease  $\langle n_{n,C} \rangle_{main}$  due to lower  $C_{cond,C}$ , Figure 14(c).

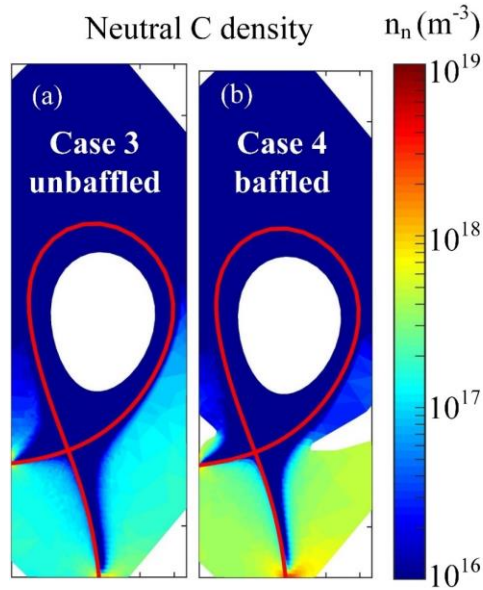


Figure 13. Neutral carbon distribution without and with baffles and with seeding (case 3 and 4 of Table II). (a) Neutral carbon density without baffles. (b) Neutral carbon density with baffles. The electron density at the upstream separatrix is  $1.5 \times 10^{19} \text{ m}^{-3}$  and the nitrogen seeding rate is  $5 \times 10^{20} \text{ s}^{-1}$ .

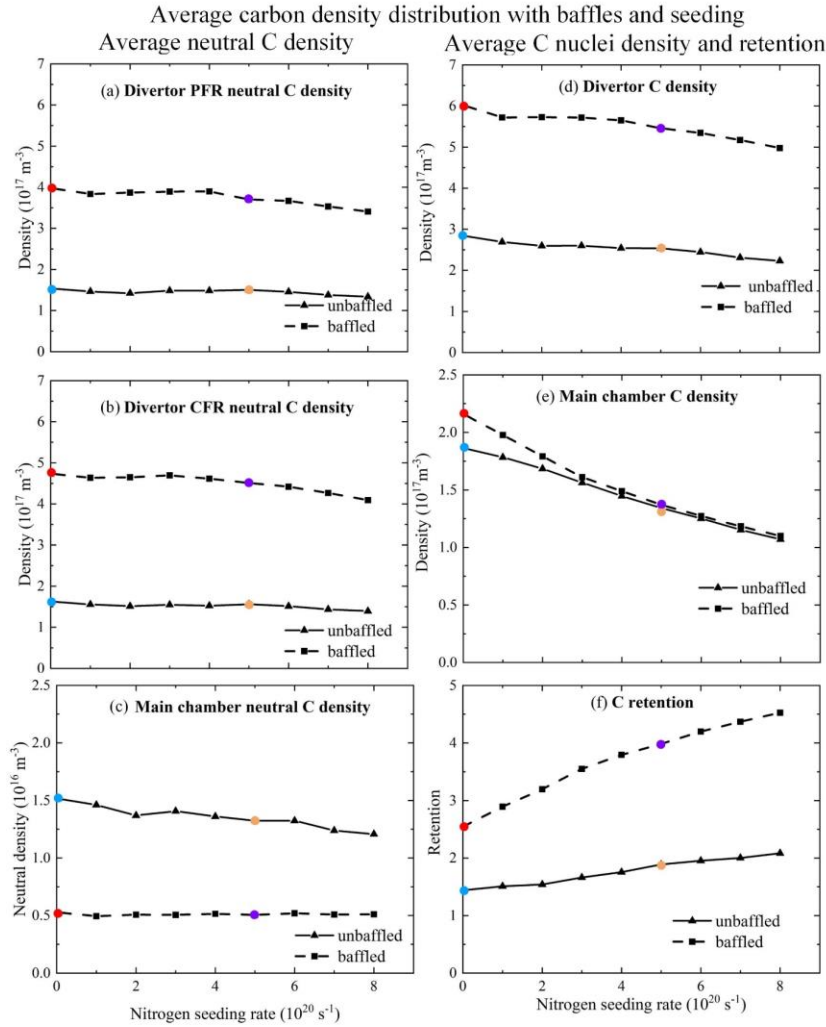


Figure 14. Average neutral carbon density in (a) Divertor PFR. (b) Divertor CFR. (c) Main chamber. Average carbon nuclei density in (d) Divertor. (e) Main chamber. The carbon retention (f). The electron density at the upstream separatrix is fixed as  $1.5 \times 10^{19} \text{ m}^{-3}$  and the colored points correspond to the four simulation cases in Table II.

Similar to nitrogen, divertor neutral carbon contributes more than 50% to the divertor carbon nuclei density  $\langle n_C \rangle_{div}$ .  $\langle n_C \rangle_{div}$  is, therefore, also higher with baffles, and slightly decreases with seeding, Figure 14(d).

Also similar to nitrogen, neutral carbon contributes little, less than 10%, to  $\langle n_C \rangle_{main}$  and observed trends of  $\langle n_C \rangle_{main}$  are due to changes of the carbon ion leakage flux from the divertor to the main chamber. Baffles cause higher target particle flux, more carbon source, and more leaked carbon ions into the main chamber, which increase  $\langle n_C \rangle_{main}$ .  $\langle n_C \rangle_{main}$  is lower with seeding due to lower target particle flux and less carbon source, Figure 14(e).

Above analyzed trends of  $\langle n_C \rangle_{div}$  and  $\langle n_C \rangle_{main}$  lead to higher  $R_C$  with baffles, Figure 14(f).  $R_C$  increases with higher seeding rate.

### 3.3.3. Analyses of the impurity radiation

Since the impurity-radiated power is proportional to the impurity density, the trends of nitrogen and carbon density distributions lead to pertinent changes in the radiated power distributions. Overall, the effects of baffles and seeding on nitrogen and carbon radiation distributions are consistent with their effects on the impurity density distributions, Figure 15.

The nitrogen radiation increases with higher seeding rate. Baffles do not change the divertor nitrogen radiation, while the core nitrogen radiation is significantly lower at high seeding level with baffles, Figure 15(e, g), (f, h). The carbon radiation decreases with higher seeding rate. Baffles increase the carbon radiation especially in the divertor region, Figure 15(a, c), (b, d).

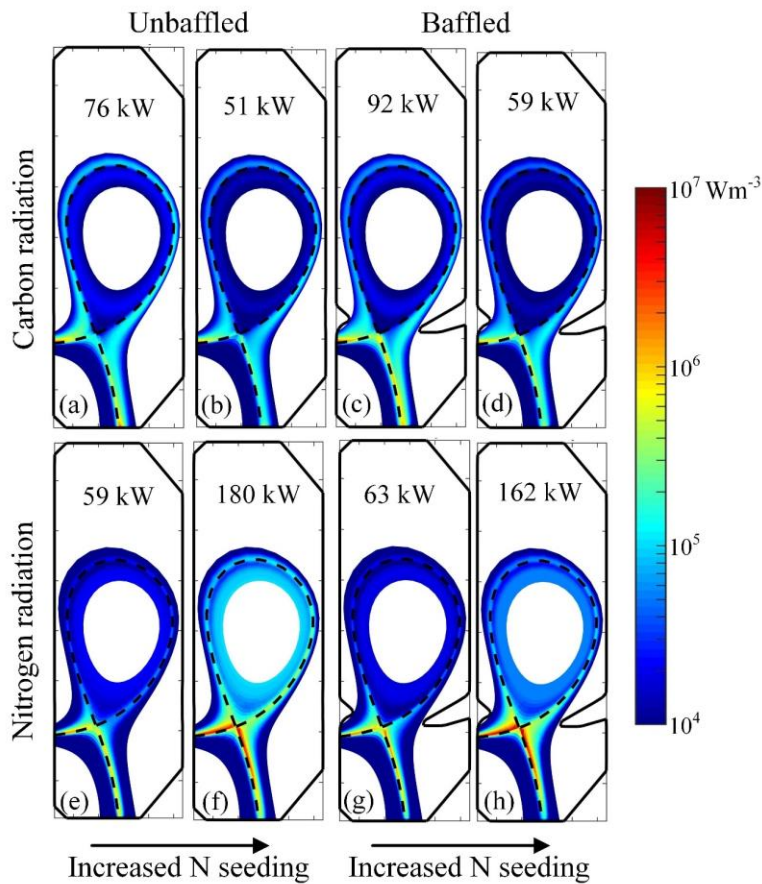


Figure 15. Impurity radiation distribution. (a)-(d) Carbon radiation. (e)-(h) Nitrogen radiation. The nitrogen seeding rate is increased from  $2 \times 10^{20}$  atom/s to  $8 \times 10^{20}$  atom/s. The electron density at the separatrix is fixed as  $1.5 \times 10^{19}$  m<sup>-3</sup>. The total radiated power of carbon and nitrogen are shown for each case.

The radiated power is integrated in the divertor and main chamber region. Adding baffles has only a negligible effects on the divertor nitrogen radiation, but considerably decreases the main chamber nitrogen radiation, Figure 16(a, b), which is consistent with the effects of baffles on  $\langle n_N \rangle_{main}$  and  $\langle n_N \rangle_{div}$ . At the highest seeding rate divertor radiation contributes 54% to the total nitrogen radiation, which increases to 64% with baffles, Figure 16(a, b).

Baffles greatly increase the divertor carbon radiation, but have less impact on the main chamber carbon radiation, Figure 16(c, d), which is consistent with the effects of baffles on  $\langle n_C \rangle_{main}$  and  $\langle n_C \rangle_{div}$ . At highest seeding rate divertor carbon radiation contributes 56% of the total carbon radiation, which increases to 71% with baffles, Figure 16(c, d). Baffles also increase the total carbon radiation by up to 28% due to increased carbon sources at the targets contributed by higher target particle flux. Nitrogen seeding decreases the overall carbon radiation due to reduced carbon sources at the targets.

Radiation from all impurity species are summed up and analyzed, Figure 16(e, f). The fraction of divertor radiation in the total radiation is 55% - 16% higher with baffles than without baffles from low to high seeding levels. The fraction of main chamber radiation is 14% - 27% lower with baffles than without baffles from low to high seeding levels. The total divertor impurity radiation increases with seeding, Figure 16(e, f).

### Changes of nitrogen and carbon radiation with baffles and seeding

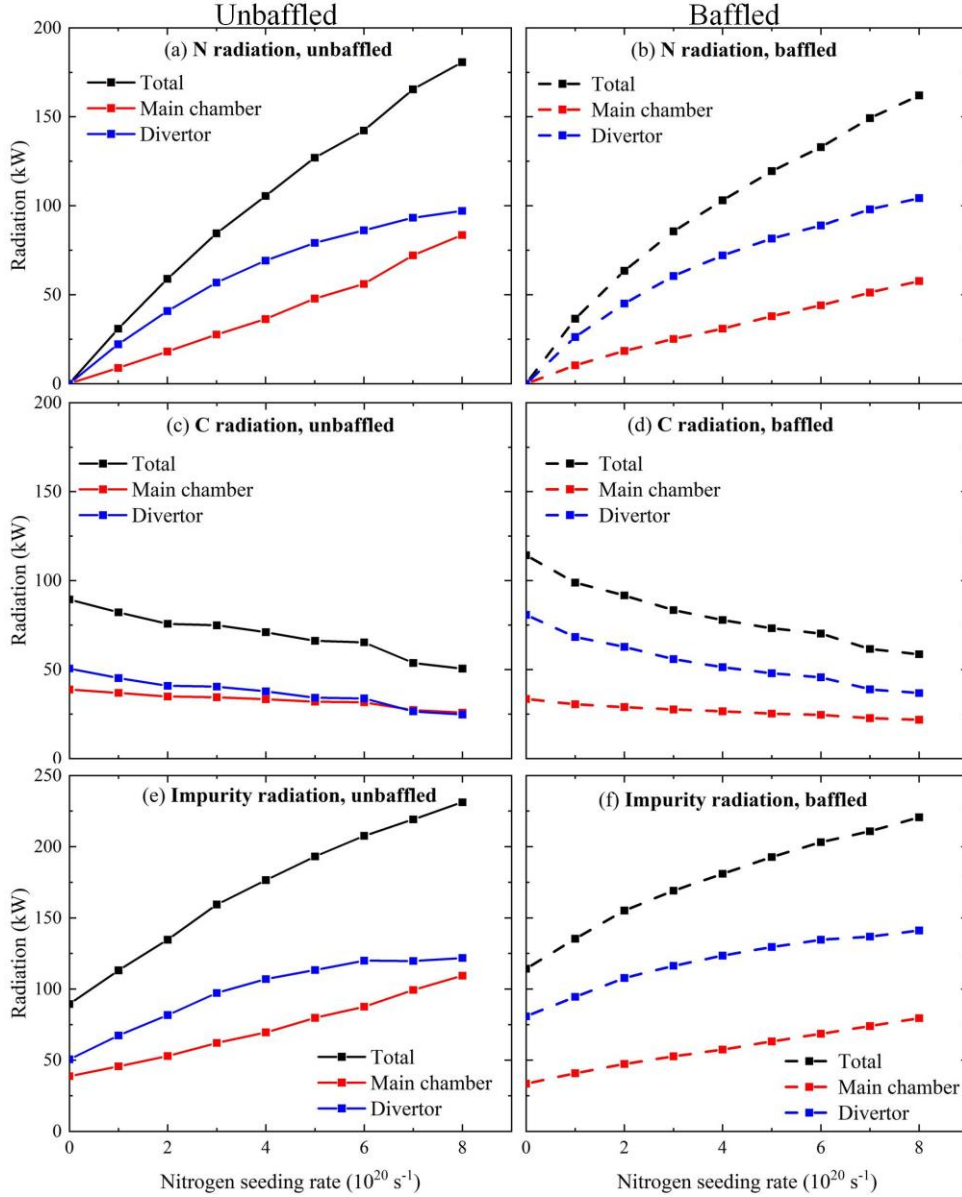


Figure 16. Nitrogen seeding scan of impurity radiation in the divertor and the main chamber regions. (a)-(b) Nitrogen radiation. (c)-(d) Carbon radiation. (e)-(f) Total impurity radiation. Region definition is shown in Figure 1(d). The electron density at the separatrix is fixed as  $1.5 \times 10^{19} \text{ m}^{-3}$ .

#### 3.3.4. Analyses of the seeding operational window

Though impurity seeding increases the divertor power dissipation, the seeding rate is limited by the core performance, which degrades with excessive core impurity concentration. The operational window that features a sufficiently large reduction of poloidal heat fluxes due to impurity radiation, without an excessive core impurity concentration, and its scaling towards a reactor, is a critical open issue. Above analyses illustrate that baffles can decrease the core nitrogen density and radiation,

suggesting a potential synergy between baffles and seeding. The operational window for nitrogen seeding with and without baffles is discussed below to demonstrate such synergy.

The upstream impurity concentration is defined as the ratio of total impurity ion density (here carbon and nitrogen) to electron density, at the upstream separatrix,  $c_{imp}^{sep} = \frac{\sum_i n_i^{i+}}{n_e}_{sep}$ . Evaluating the impurity concentration at the upstream separatrix instead of in the core region avoids a dependence on the definition of the computational grid.

The operational window of seeded detachment is defined as the conditions where the peak outer target temperature is below 5 eV, and  $c_{imp}^{sep}$  is within tolerable levels, Figure 17. While a maximum tolerable  $c_{imp}^{sep}$  is difficult to define, lower values are generally more favorable. The baffled divertor features significantly lower core pollution for the same plasma temperature at the targets than the unbaffled divertor. Higher input power shifts the  $c_{imp}^{sep} - T_{ot,max}$  to higher  $T_{ot,max}$  (not shown). The analyses of the seeding operational window show that baffles can significantly decrease the upstream nitrogen concentration while keeping the divertor detached, which widens the seeding operational window.

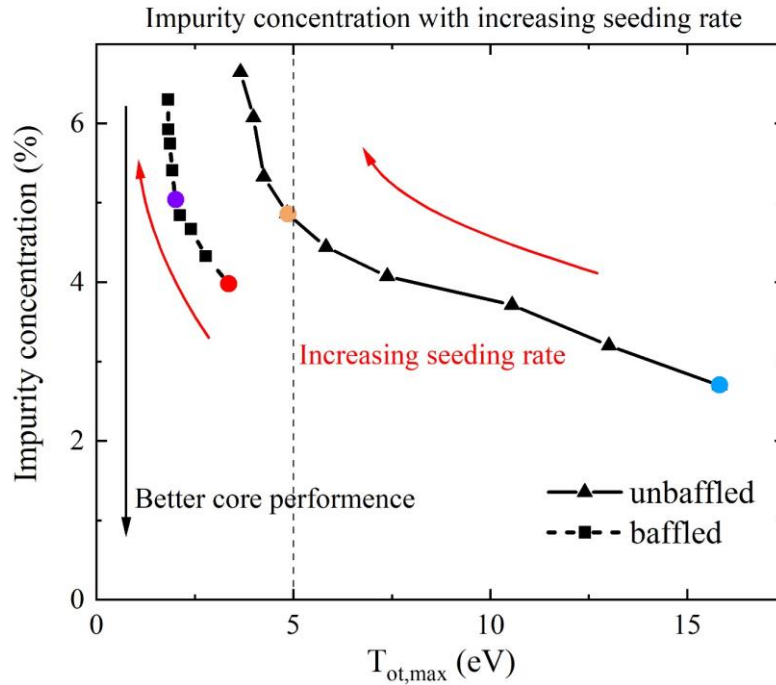


Figure 17. The impurity concentration at the separatrix as function of peak outer target temperature, obtained with nitrogen seeding rate from 0 to  $8 \times 10^{20} \text{ s}^{-1}$ . The electron density at separatrix is fixed as  $1.5 \times 10^{19} \text{ m}^{-3}$  and the colored points correspond to the four simulation cases in Table II. Detachment threshold is marked by the vertical dashed line.

#### 4. COMPARISON WITH TCV EXPERIMENTS

In this section, SOLPS-ITER simulations, including target plasma parameters, neutral and radiation distributions, are compared with TCV experiments. The comparison seeks to improve the understanding of experimental trends and identify potential reasons for discrepancies, rather than aiming for quantitative agreement. Key predictions to verify in TCV are:

1) Target parameters. Baffles increase the target electron density and particle flux, decreases the target electron temperature and heat flux. Seeding decreases the target electron temperature, particle flux and heat flux, but does not change the target electron density.

2) Neutral density and compression. Baffles increase the divertor neutral density and neutral compression, decrease the main chamber neutral density.

3) Impurity radiation. Baffles increase the radiation fraction of the nitrogen in the divertor, and increase the carbon radiation in the divertor. Seeding increases the nitrogen radiation, and decreases the carbon radiation. Both baffles and seeding increase the total divertor impurity radiation.

#### 4.1. Criteria for comparison

The comparison is based on Ohmic L-mode TCV discharges with a plasma current of 250 kA and line-averaged electron densities of approximately  $3.7 \pm 0.2 \times 10^{19} \text{ m}^{-3}$ . The SOLPS upstream electron density is matched with the Thomson scattering measurement of these discharges. Nitrogen seeding starts at 0.85s, with a linearly increasing rate until a disruption occurs, Figure 18. While the radiated power and seeding rate at the disruption vary among identically programmed discharges, all discharges show an increase of the radiation with increasing  $\text{N}_2$  seeding rate.

### Time traces of the N-seeded TCV discharges

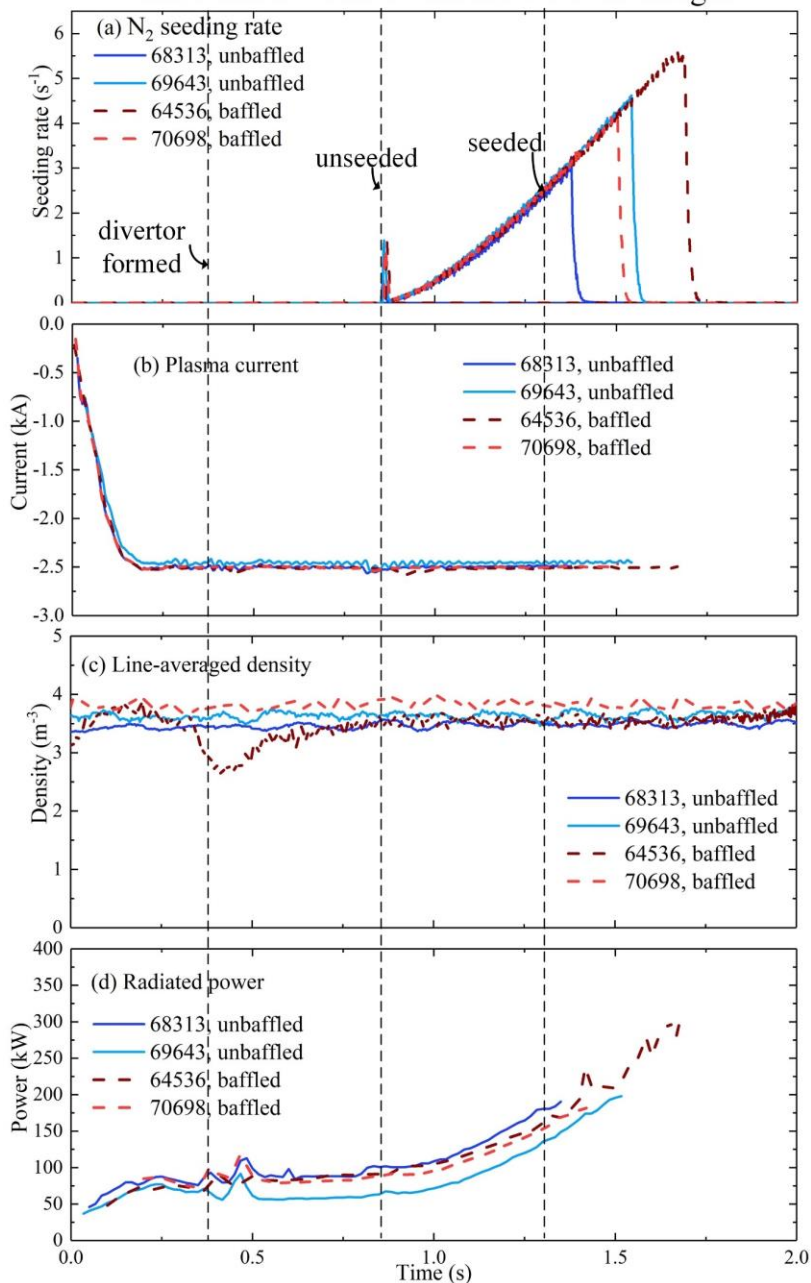


Figure 18. (a) Nitrogen seeding rate, (b) plasma current, (c) line-averaged density and (d) radiated power in unbaffled (solid) and baffled (dashed) TCV discharges. The divertor formation is marked by a first dashed line. The times that correspond to the unseeded and seeded ( $5 \times 10^{20}$  atom/s) cases in the comparison are marked by another two dashed lines.

The nitrogen seeding rate is used as the ordering parameter for the comparison of simulations and experiments. This approach assumes that the seeding rate ramp is sufficiently slow to result in quasi-stationary plasma states that can be compared to stationary SOLPS simulations. While faster seeding ramps lead to a systematic error, they should still show the same trends observed in simulation.

## 4.2. Comparison of target profiles

The outer target electron density,  $n_{e,ot}$ , temperature,  $T_{e,ot}$ , and particle flux,  $\Gamma_{ot}$ , are measured by wall-embedded Langmuir probes (LP). The heat flux,  $q_{ot}$ , is measured by an infrared thermography diagnostic (IR). The wall-embedded Langmuir probes directly measure the target ion saturation currents  $J_{ot} = e\Gamma_{ot}$ , and their I-V curves provide estimates of the  $T_{e,ot}$ . The value of  $n_{e,ot}$  is derived from  $J_{ot}$  and  $T_{e,ot}$  [52].

The target ion saturation currents reflect the difference between volumetric ion sources and sinks. The measured trend that target currents increase with baffles and decrease with seeding is consistent with the SOLPS predictions, Figure 2 and Figure 19. In all cases, SOLPS overestimates the target currents by approximately a factor of two. This is related to an overestimated ionization source, which is also reflected in an overestimated divertor neutral pressure, to be discussed in Section 4.3. The double-peak in the measured target current is not seen in simulations, likely due to the neglect of particle drifts. The double-peaked target density profile with drifts activated were previously observed in TCV simulations with the UEDGE [53], and SOLPS codes [54].

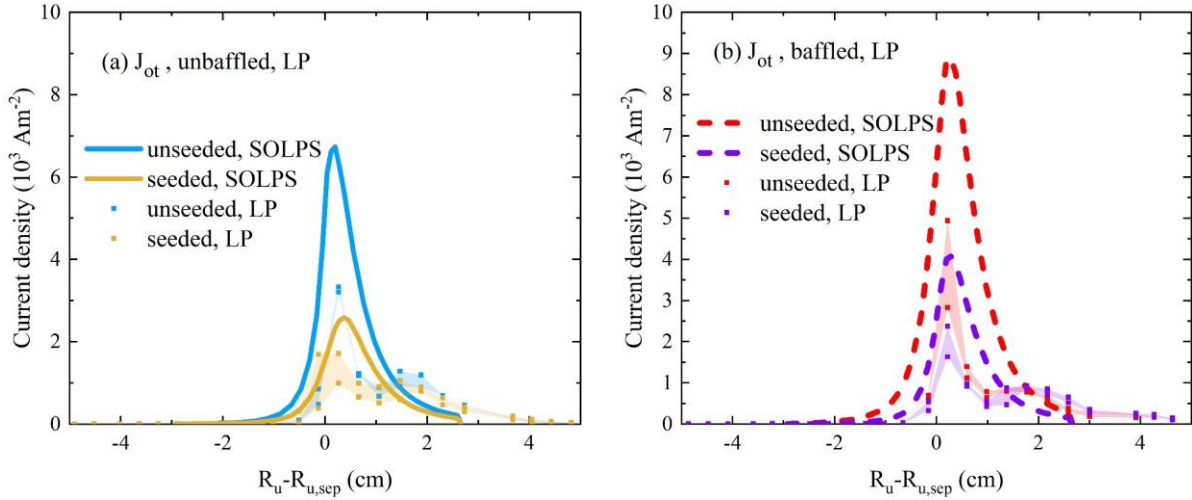


Figure 19. Comparison of measured and predicted outer particle currents in the (a) unbaffled and (b) baffled TCV configurations. The currents are taken from wall-embedded Langmuir probes, and seeding rate is  $5.0 \times 10^{20} \text{ s}^{-1}$  in the seeded cases. Shaded areas represent the upper and lower limit of the LP measurements for the four TCV discharges shown in section 4.1. Each point of the measurement corresponds to the current and  $R_u - R_{u,sep}$  of one particular probe averaged over a time interval of 5 ms.

Target electron density and temperature are key parameters which strongly influence the reaction rates in the divertor. Matching the simulation target density and temperature with the TCV experiment is, therefore, essential to evaluate the reliability of the predictions. The decrease of target temperature by both seeding and baffles is shown in both SOLPS predictions

and LP measurement, Figure 20. The lowest target temperature with seeding and baffles is well reproduced in LP measurement. For the unbaffled, seeded case, SOLPS somewhat underestimates the target temperature measured with LPs.

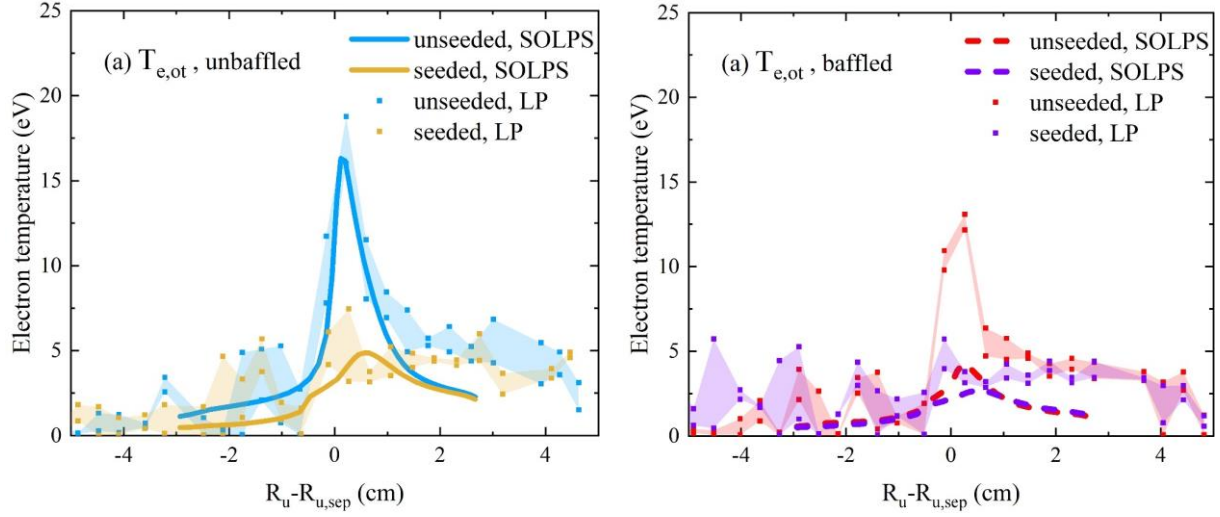


Figure 20 . Comparison of measured and predicted outer target electron temperatures in the (a) the unbaffled and (b) baffled TCv configurations. Temperature profiles are taken from wall-embedded Langmuir probes, and seeding rate is  $5.0 \times 10^{20} \text{ s}^{-1}$  in the seeded cases. Shaded areas represent the upper and lower limit of the LP measurements for the four TCv discharges shown in section 4.1. Each point of the measurement corresponds to the temperature and  $R_u - R_{u,sep}$  of one particular probe averaged over a time interval of 5 ms.

The target electron density is derived from Langmuir probes, based on  $n_t = \frac{J_t}{ec_{s,t}}$ , with  $J_t$  the saturation current density and  $c_{s,t}$  the ion sound speed. The increase of target electron density by baffles is observed in both simulation and experiment, with SOLPS predictions higher than the LP measurements for both baffled and unbaffled conditions, Figure 21, as already observed in previous work that included drifts [30]. The trend that the target electron density is insensitive to the seeding is also observed in both simulation and experiment, Figure 21. However, the “double peak” in the measured density profile is not recovered in the simulations and may require the inclusion of drifts. The simulations also generally overestimate  $n_{ot}$ , consistent with the general overestimation of  $\Gamma_{ot}$ .

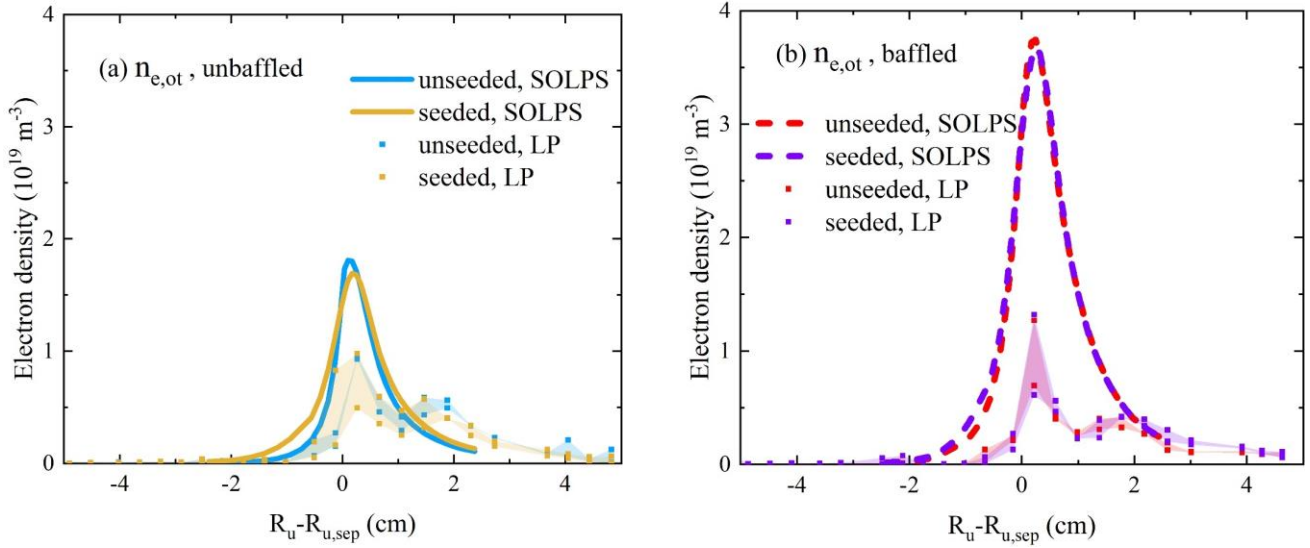


Figure 21. Comparison of measured and predicted outer target electron density measured by the Langmuir probe with zero seeding rate. (a) without baffles (b) with baffles. Shaded areas represent the upper and lower limit of the LP measurements for the four TCV discharges shown in section section 4.1. Each point of the measurement corresponds to the density and  $R_u - R_{u,sep}$  of one particular probe averaged over a time interval of 5 ms.

Target heat fluxes are measured using TCV's IR thermography diagnostic. Here the heat flux due to neutrals and radiation is included in the simulation results. The trends that baffles and seeding both decrease the target heat flux are consistent in SOLPS simulations and the IR measurements, Figure 22(a, b). SOLPS simulations predict lower target heat flux than the IR measurement except for the unseeded, unbaffled case. The underestimated target heat flux by SOLPS is consistent with the underestimated  $J_{ot}$  and  $T_{e,ot}$ .

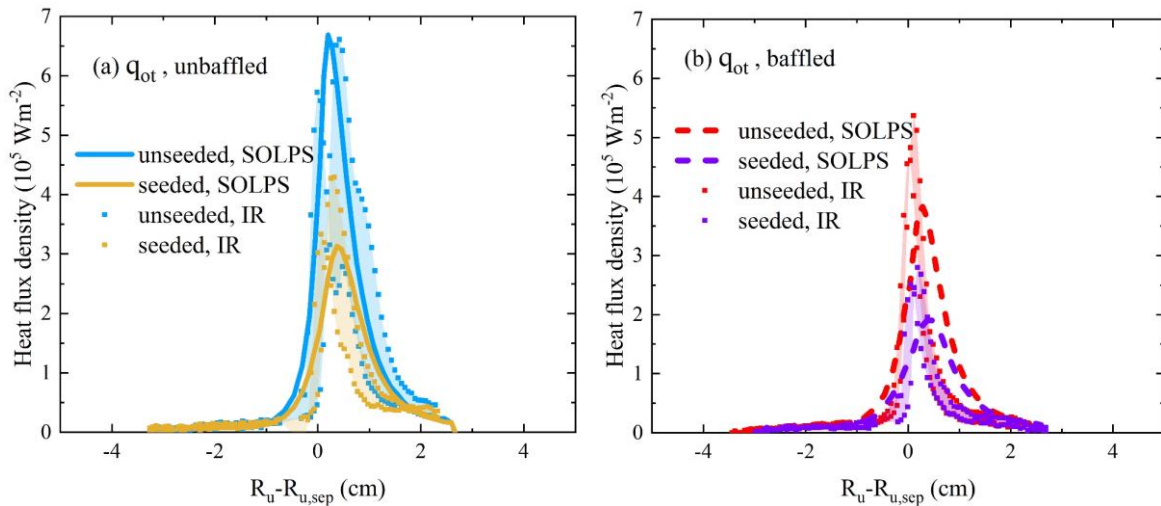


Figure 22. Comparison of IR-measured and simulated outer target plasma heat fluxes in the (a) unbaffled and (b) baffled TCV configurations. The nitrogen seeding rate in the seeded cases is  $5.0 \times 10^{20} \text{ atom s}^{-1}$ . Shaded areas represent the upper and lower limit of the IR measurements

for the four TCV discharges shown in section 4.1. Each point of the measurement corresponds to the heat flux and  $R_u - R_{u,sep}$  of one particular probe averaged over a time interval of 5 ms.

### 4.3. Comparison of neutral pressure

The detachment is primarily achieved by transferring momentum from the plasma to neutrals. The behavior of neutrals significantly influences the SOL properties. Baratron pressure gauges are installed in TCV to monitor the neutral pressure in divertor. Since the baratron gauges cannot operate under high magnetic field, they are located outside the toroidal field coils at the end of long extension tubes. The neutral conductance of the tubes introduces a nonnegligible time delay. Collisions of neutrals with the tube lead to a pressure drop along the tube, which must be taken into account in the comparison with SOLPS. The employed model was originally proposed for interpreting neutral dynamics in Alcator C-Mod [55] and is also applied to TCV modeling [28]

Baratron gauge measurements and SOLPS simulations, both, show a significant increase of divertor neutral pressure by baffles, while the divertor neutral pressure is independent of the seeding, Figure 23(a, b)<sup>4</sup>. SOLPS overestimates the neutral pressure by a factor of approximately two without baffles and by a factor of 3-4 with baffles, indicating that the increase of divertor neutral pressure by baffles is overestimated by SOLPS. This overestimation of neutral pressure by simulation is consistent with abovementioned target profiles, i.e. simulation gives a denser and colder divertor than measured from diagnostics and similar to previous findings without nitrogen seeding [30]. The compression is not measured as the outer board mid-plane pressure is low, and is beyond the baratron gauge measurement limit.

---

<sup>4</sup> The oscillation of baratron pressure measurements in the unbaffled discharges is thought to be caused by mechanical vibrations of the baratron gauge support

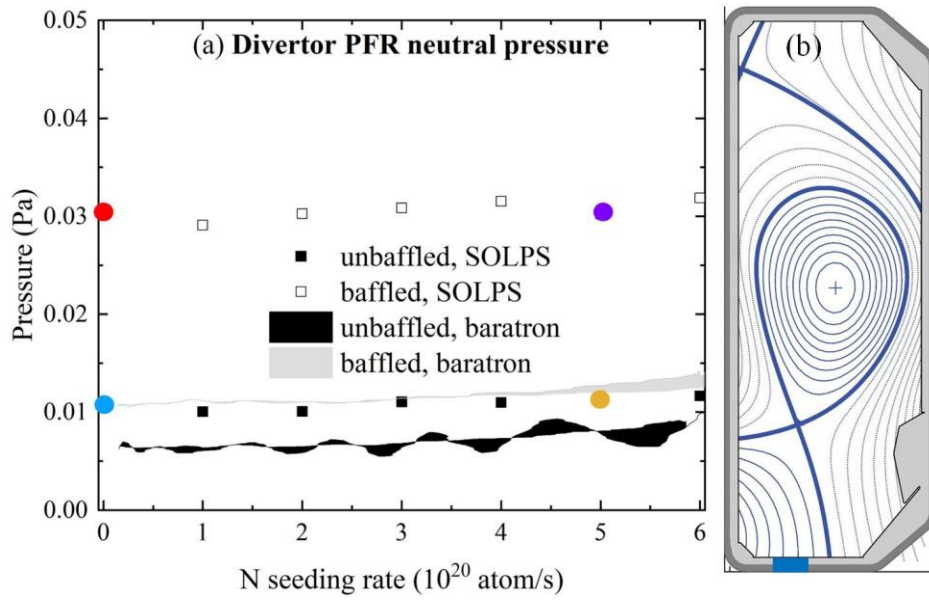


Figure 23 Comparison of measured and simulated neutral pressure in the un baffled (solid) and baffled (dashed) TC configurations. (a) Divertor PFR neutral pressure measured by the baratron gauge. (b) Locations of divertor baratron gauge in TC. Shaded areas represent the upper and lower limit of the baratron gauges. Each point of the measurement corresponds to the pressure averaged over a time interval of 5 ms.

#### 4.4 Comparison of radiated power

The radiated power distribution, measured TCV bolometers (BOLO) and RADCAM system [56], and the Divertor spectroscopy system (DSS), are used to validate the observed effects of baffles and seeding on the impurity radiation.

In the analyzed discharges, the plasma radiation measurements along 64 chords of the legacy bolometers reconstruct the spatial radiation distribution. The camera sets are located at the vessel top, the vessel bottom and three lateral positions in the low-field side of the tokamak at the same toroidal location, Figure 24(e). To compare with the measurement, the simulated radiated power density is integrated along the link-of-sight of each chord, similar to previous work [30]. Baffles and seeding both increase the radiation, most obviously in the chords 41-64 (magenta and yellow), where SOLPS overpredicts the measurements by approximately a factor of two. Such discrepancies were also observed for TC simulation using SOLPS code without seeding [30].

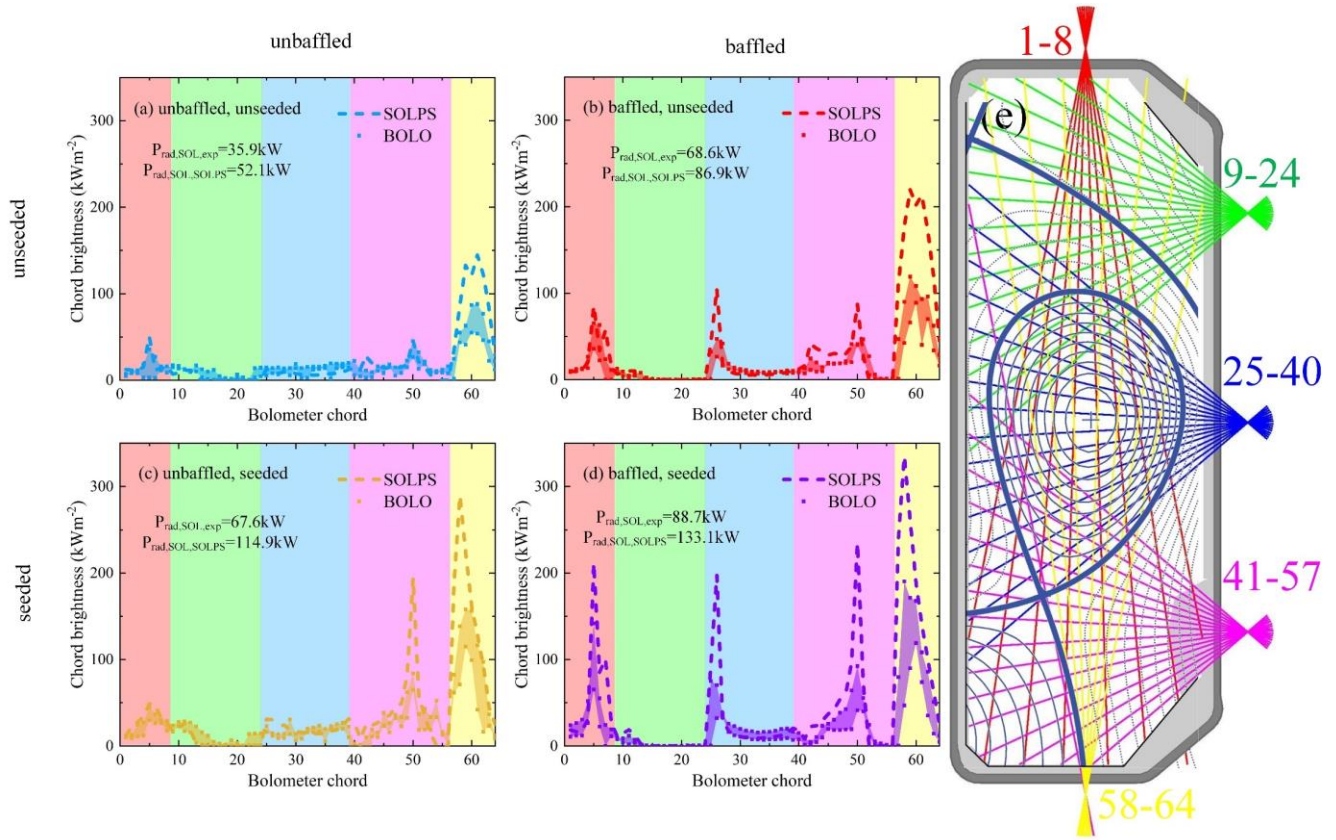


Figure 24. Comparison of measured and simulated bolometer chord brightness in the (a) unbaffled, unseeded case, (b) unbaffled, seeded case, (c) baffled, unseeded case and (d) baffled, seeded cases. The seeding rate in the seeded cases is  $5.0 \times 10^{20} \text{ s}^{-1}$ . (e) Bolometer coverage. Shaded zones in (a)-(d) correspond to BOLO cameras at top (red), upper lateral (green), midplane lateral (blue), lower lateral (magenta), and bottom (yellow) positions. Shaded areas represent the upper and lower limit of the BOLO measurements for the four TCV discharges shown in section 4.1. Each point of the measurement corresponds to the brightness averaged over a time interval of 5 ms.

The 2D radiated power distribution can be obtained from the BOLO measurement by performing the tomographic inversions. Integrating the obtained radiation distribution over the divertor region (same definition as in section 3.2), the increase of total divertor radiation by increasing the seeding rate and adding the baffles is confirmed, Figure 25. The trends of measured radiation with baffles and seeding are consistent with the SOLPS prediction, through the SOLPS simulations predict slightly stronger radiation than measured at high seeding levels.

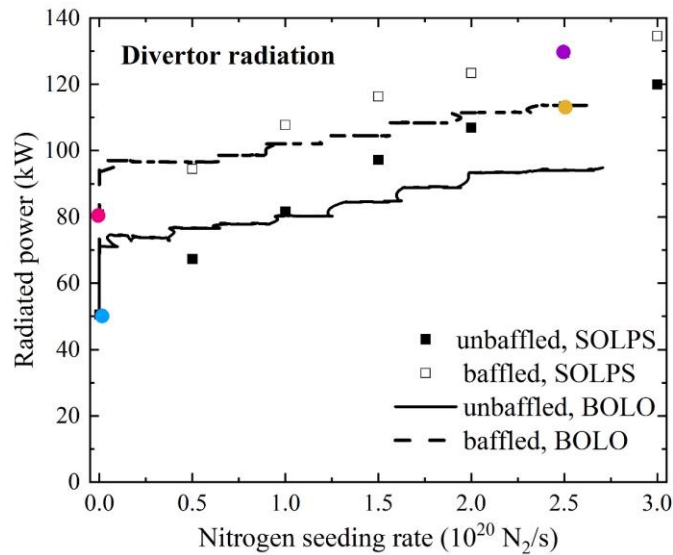


Figure 25. Comparison of the measured and simulated divertor radiation with varying nitrogen seeding rate. The SOLPS datapoints with various seeding rates are matched with the time axis according to Figure 18(a). The colored points correspond to the four simulation cases in Table II. Only measurement of one discharge is available for un baffled and baffled divertor (69643 and 70698).

The divertor spectroscopy system (DSS) in TCv measures the spectrally resolved divertor emission. By comparing the DSS measurements with the synthetic diagnostic signals in SOLPS, consistency of impurity emission lines can be surveyed to validate the changes of carbon and nitrogen emission with seeding and baffles. A more complete descriptions of the DSS system and the calculation of synthetic DSS signals in SOLPS are available in [31, 57]. Here line-integrated intensity of each DSS chord for CII 426.8 nm line emitted by carbon ions, and NII 399.5 nm line emitted by the nitrogen ions, are inspected.

The SOLPS predictions generally overpredict the CII emission by approximately a factor of two to four. DSS measurements show that baffles increase the divertor CII emission only in the unseeded cases, Figure 26, whereas the SOLPS simulations baffles increase the divertor CII emission in both, seeded and unseeded cases. DSS measurements also show that seeding decreases the divertor CII emission in the baffled cases, which is less visible in the un baffled cases, Figure 24. SOLPS simulations show that seeding decreases the CII emission for both un baffled and baffled cases. The baffled, unseeded case shows strongest divertor carbon radiation in both DSS measurement and SOLPS predictions.

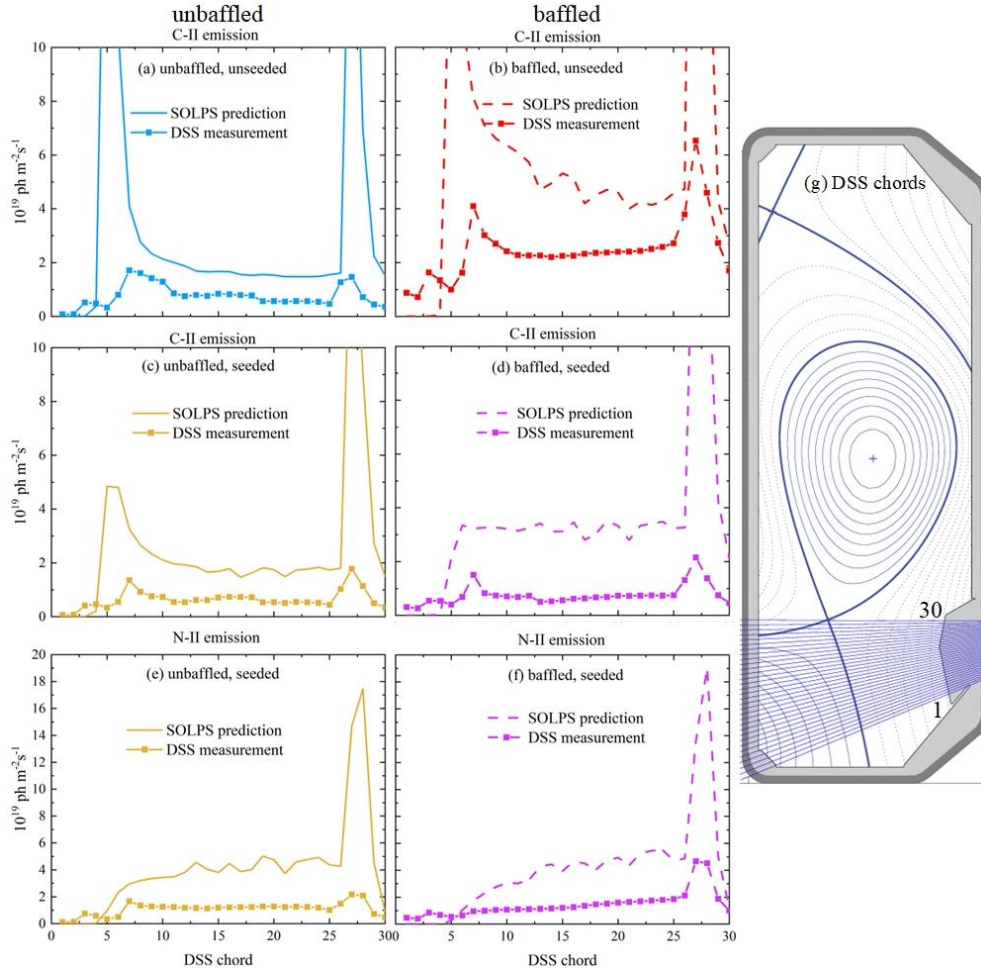


Figure 26. CII (426.8 nm) emission (a-d) and NII (398.5 nm) emission (e-f) comparison between DSS and synthetic diagnostic for (a) unbauffed, unseeded case, (b) baffled, unseeded case, (c) unbauffed, seeded case, (d) baffled, seeded case, (e) unbauffed, seeded case, and (f) baffled, seeded cases. (g) DSS chord number and line of sight. The seeding rate is  $5.0 \times 10^{20} \text{ s}^{-1}$  in the seeded cases. Only measurement of one discharge is available for unbauffed and baffled divertor (69643 and 70698).

Similarly, SOLPS simulations generally overestimate the NII emission by a factor of three to five. DSS measurements also confirm that baffles can increase the divertor NII emission, Figure 25. Seeding increases the NII emission, which is trivial and not shown here.

#### 4.5. Summary of the simulation-experiment comparison

The main observations are:

- 1) The comparison verifies that baffles increase the target electron density and particle flux, while decreasing the target electron temperature and heat flux. In addition, seeding decreases the target electron temperature, particle flux and heat flux,

but does not change the target electron density. SOLPS generally overpredicts the measured target density and, hence, particle fluxes.

2) The comparison verifies that baffles significantly increase the divertor neutral pressure, while the divertor neutral pressure is not affected by seeding. SOLPS generally overpredicts the measured neutral pressures.

3) The comparison verifies that baffles and seeding both increase the divertor radiation. It is confirmed that baffles increase the CII emission when there is no seeding, while seeding decreases the CII emission in baffled divertors. Baffles can increase the divertor NII emission. SOLPS generally overpredicts the radiated power and the CII, NII emissions.

Potential reasons that cause the discrepancies in the comparison as well as the possible measures to fix them in future works are briefly discussed. First, SOLPS-ITER simulation is based on results in equilibrium, whereas the nitrogen seeding rate is dynamic and ramps up in TCV discharge. This can be corrected by choosing other ordering parameters in future comparison, such as target temperature. Second, the nitrogen recycling coefficient affects the amount of nitrogen in the TCV chamber for a given seeding rate. The uncertainty in the nitrogen recycling coefficient, therefore, directly affects the nitrogen content. The strategy for choosing the nitrogen recycling coefficient can be revised in future comparison. In addition, the discrepancies may be further decreased by using different transport coefficients and including drifts.

The systematic discrepancies of colder and denser, divertor target plasmas with higher neutral pressure, as predicted by SOLPS simulations than TCV measurements, were also observed in the comparison of unseeded TCV discharges with SOLPS simulation [30]. Recent studies highlighted a stronger importance of plasma-molecule interaction with systematic errors in some of the included reaction cross sections in SOLPS, which is one of the possible explanations for above discussions [40]. The cause of the mismatched divertor properties remains elusive, and improved diagnostics and SOLPS modeling are in active progress to further address this issue.

## 5. CONCLUSIONS

The interplay between baffling and nitrogen seeding in L-mode TCV divertor detachment was investigated with SOLPS-ITER simulations and tested with TCV experiments. The simulation-experiment comparison shows that outer target electron temperature and heat flux are significantly reduced by both baffles and seeding, and their contributions are cumulative. Baffles increase the target particle flux and density, whereas seeding decreases the target particle flux.

The simulation-experiment comparison also verifies that baffles significantly increase the divertor neutral pressure. The roles of baffles on neutral distribution are explained by a schematic neutral transport model with SOLPS-ITER simulations. Baffles decrease the neutral conductance from the divertor to the main chamber, which directly increase the divertor neutral pressure.

SOLPS-ITER simulations further reveal the effects of baffles and seeding on the impurity distribution. Baffles are shown to increase the carbon density in both divertor and main chamber due to higher target particle flux. Baffles increase the nitrogen impurity retention and decrease the main chamber nitrogen density at high seeding levels. This is explained by the changes of main ion flow by baffles and the changes of ion temperature by baffles and seeding, while the direct effects of baffles on nitrogen neutrals is insignificant for the main chamber nitrogen density. An experimental verification would require main chamber N measurements, which are not available on TCV. The changes of impurity density distribution affect the impurity radiation accordingly. The simulation-experiment comparison shows that baffles and seeding both increase the divertor radiation. Baffles increase both the divertor CII emission and NII emission, whereas seeding decreases the divertor CII emission and increases the NII emission.

The first comparison of SOLPS-ITER simulations and TCV experiments with baffles and seeding shows qualitative consistency in trend, though the simulations predict a colder and denser divertor compared with experiments. The discrepancies are expected to be reduced in future works by, e.g. including drifts, refining choices of transport coefficient in simulation, optimizing the strategy for simulation-experiment comparison, etc. The present work increases the confidence of using SOLPS-ITER simulations for the next TCV divertor upgrade.

## ACKNOWLEDGMENTS

This work has been carried out within the framework of the EUROfusion Consortium, via the Euratom Research and Training Programme (Grant Agreement No. 101052200— EUROfusion) and funded by the Swiss State Secretariat for Education, Research and Innovation (SERI). Views and opinions expressed are however those of the author(s) only and do not necessarily reflect those of the European Union, the European Commission, or SERI. Neither the European Union nor the European Commission nor SERI can be held responsible for them. This work was supported in part by the Swiss National Science Foundation.

## DATA AVAILABILITY STATEMENT

The data that support the findings of this study are available from the corresponding author upon reasonable request.

## REFERENCES

- [1] Stangeby P C 2018 Basic physical processes and reduced models for plasma detachment *Plasma Physics and Controlled Fusion* **60** 044022
- [2] Leonard A W 2018 Plasma detachment in divertor tokamaks *Plasma Physics and Controlled Fusion* **60** 044001
- [3] Krasheninnikov S, Smolyakov A and Kukushkin A 2020 *On the Edge of Magnetic Fusion Devices*, (Cham: Springer International Publishing) pp 1-12
- [4] Kallenbach A, Bernert M, Dux R, Casali L, Eich T, Giannone L, Herrmann A, McDermott R, Mlynek A, Müller H W, Reimold F, Schweinzer J, Sertoli M, Tardini G, Treutterer W, Viezzer E, Wenninger R, Wischmeier M and the A U T 2013 Impurity seeding for tokamak power exhaust: from present devices via ITER to DEMO *Plasma Physics and Controlled Fusion* **55** 124041
- [5] Wischmeier M 2015 High density operation for reactor-relevant power exhaust *Journal of Nuclear Materials* **463** 22-9
- [6] Soukhanovskii V A 2017 A review of radiative detachment studies in tokamak advanced magnetic divertor configurations *Plasma Physics and Controlled Fusion* **59** 064005
- [7] Pitts R A, Bonnin X, Escourbiac F, Frerichs H, Gunn J P, Hirai T, Kukushkin A S, Kaveeva E, Miller M A, Moulton D, Rozhansky V, Senichenkov I, Sytova E, Schmitz O, Stangeby P C, De Temmerman G, Veselova I and Wiesen S 2019 Physics basis for the first ITER tungsten divertor *Nuclear Materials and Energy* **20** 100696
- [8] Kallenbach A, Coster D, Fuchs J C, Guo H Y, Haas G, Herrmann A, Horton L D, Ingesson L C, Maggi C F, Matthews G F, Monk R D, Neuhauser J, Ryter F, Schweinzer J, Stober J, Suttrop W, Team A U and Team J E T 1999 Closed divertor operation in ASDEX Upgrade and JET *Plasma Physics and Controlled Fusion* **41** B177
- [9] Sang C F, Stangeby P C, Guo H Y, Leonard A W, Covele B, Lao L L, Moser A L and Thomas D M 2016 SOLPS modeling of the effect on plasma detachment of closing the lower divertor in DIII-D *Plasma Physics and Controlled Fusion* **59** 025009
- [10] Guo H Y, Wang H Q, Watkins J G, Casali L, Covele B, Moser A L, Osborne T, Samuell C M, Shafer M W, Stangeby P C, Thomas D M, Boedo J, Buttery R J, Groebner R, Hill D N, Holland L, Hyatt A W, Jaervinen A E, Kellman A, Lao L L, Lasnier C J, Leonard A W, Murphy C, Ren J, Sang C F, Sontag A C, Taylor T S and the D-D T 2019 First experimental tests of a new small angle slot divertor on DIII-D *Nuclear Fusion* **59** 086054
- [11] Casali L, Eldon D, Boedo J A, Leonard T and Covele B 2020 Neutral leakage, power dissipation and pedestal fueling in open vs closed divertors *Nuclear Fusion* **60** 076011
- [12] Hofmann F, Lister J B, Anton W, Barry S, Behn R, Bernel S, Besson G, Buhlmann F, Chavan R, Corboz M, Dutch M J, Duval B P, Fasel D, Favre A, Franke S, Heym A, Hirt A, Hollenstein C, Isoz P, Joye B, Llobet X, Magnin J C, Marletaz B, Marmillod P, Martin Y, Mayor J M, Moret J M, Nieswand C, Paris P J, Perez A, Pietrzyk Z A, Pitts R A, Pochelon A, Rage R, Sauter O, Tonetti G, Tran M Q, Troyon F, Ward D J and Weisen H 1994 Creation and control of variably shaped plasmas in TCV *Plasma Physics and Controlled Fusion* **36** B277
- [13] Lipschultz B, LaBombard B, Marmor E S, Pickrell M M, Terry J L, Watterson R and Wolfe S M 1984 Marfe: an edge plasma phenomenon *Nuclear Fusion* **24** 977
- [14] Sytova E, Pitts R A, Kaveeva E, Bonnin X, Coster D, Rozhansky V, Senichenkov I, Veselova I, Voskoboinikov S and Reimold F 2019 Comparing N versus Ne as divertor radiators in ASDEX-upgrade and ITER *Nuclear Materials and Energy* **19** 72-8
- [15] Bernert M, Wischmeier M, Huber A, Reimold F, Lipschultz B, Lowry C, Brezinsek S, Dux R, Eich T, Kallenbach A, Lebschy A, Maggi C, McDermott R, Pütterich T and Wiesen S 2017 Power exhaust by SOL and pedestal radiation at ASDEX Upgrade and JET *Nuclear Materials and Energy* **12** 111-8
- [16] Pan O, Bernert M, Lunt T, Cavedon M, Kurzan B, Wiesen S, Wischmeier M, Stroth U and Upgrade Team t A 2023 SOLPS-ITER simulations of an X-point radiator in the ASDEX Upgrade tokamak *Nuclear Fusion* **63** 016001
- [17] Wang H Q, Guo H Y, Petrie T W, Leonard A W, Thomas D M and Watkins J G 2017 Effects of low-Z and high-Z impurities on divertor detachment and plasma confinement *Nuclear Materials and Energy* **12** 942-7
- [18] Février O, Theiler C, Harrison J R, Tsui C K, Verhaegh K, Wüthrich C, Boedo J A, De Oliveira H, Duval B P, Labit B, Lipschultz B, Maurizio R and Reimerdes H 2020 Nitrogen-seeded divertor detachment in TCV L-mode plasmas *Plasma Physics and Controlled Fusion* **62** 035017

- [19] Raj H, Theiler C, Thornton A J, Février O, Gorno S, Bagnato F, Blanchard P, Colandrea C, de Oliveira H, Duval B P, Labit B, Perek A, Reimerdes H, Sheikh U A, Vallar M and Vincent B 2022 Improved heat and particle flux mitigation in high core confinement, baffled, alternative divertor configurations in the TCV tokamak *Nuclear Fusion*
- [20] Bernert M, Wiesen S, Février O, Kallenbach A, Koenders J T W, Sieglin B, Stroth U, Bosman T O S J, Brida D, Cavedon M, David P, Dunne M G, Henderson S, Kool B, Lunt T, McDermott R M, Pan O, Perek A, Reimerdes H, Sheikh U, Theiler C, van Berkel M, Wijkamp T and Wischmeier M 2023 The X-Point radiating regime at ASDEX Upgrade and TCV *Nuclear Materials and Energy* **34** 101376
- [21] Alberto L 2001 Effects of divertor geometry on tokamak plasmas *Plasma Physics and Controlled Fusion* **43** R183
- [22] Moser A L, Leonard A W, McLean A G, Wang H Q and Watkins J G 2019 The effect of divertor closure on detachment onset in DIII-D *Nuclear Materials and Energy* **19** 67-71
- [23] Tao Y Q, Xu G S, Yang Q Q, Yan N, Jia G Z, Meng L Y, Liu S C, Chen L, Yu Y W, Gao W, Wang Y M, Wang L, Zang Q and Gao S L 2021 Impact of divertor closure on edge plasma behavior in EAST H-mode plasmas *Plasma Physics and Controlled Fusion* **63** 065004
- [24] Février O, Reimerdes H, Theiler C, Brida D, Colandrea C, De Oliveira H, Duval B P, Galassi D, Gorno S, Henderson S, Komm M, Labit B, Linehan B, Martinelli L, Perek A, Raj H, Sheikh U, Tsui C K and Wensing M 2021 Divertor closure effects on the TCV boundary plasma *Nuclear Materials and Energy* **27** 100977
- [25] Fasoli A, Reimerdes H, Alberti S, Baquero-Ruiz M, Duval B P, Havlikova E, Karpushov A, Moret J M, Toussaint M, Elaian H, Silva M, Theiler C, Vaccaro D and the T C V t 2020 TCV heating and divertor upgrades *Nuclear Fusion* **60** 016019
- [26] Galassi D, Reimerdes H, Theiler C, Wensing M, Bufferand H, Ciralo G, Innocente P, Marandet Y, Tamain P, Labit B and Coda S 2021 Numerical investigation of optimal divertor gas baffle closure on TCV *Plasma Physics and Controlled Fusion* **62** 115009
- [27] Fasoli A, Reimerdes H, Alberti S, Baquero-Ruiz M, Duval B P, Havlikova E, Karpushov A, Moret J M, Toussaint M, Elaian H, Silva M, Theiler C and Vaccaro D 2019 TCV heating and divertor upgrades *Nuclear Fusion* **60** 016019
- [28] Wensing M, Duval B P, Février O, Fil A, Galassi D, Havlickova E, Perek A, Reimerdes H, Theiler C, Verhaegh K, Wischmeier M, the E M S T t and the T C V t 2019 SOLPS-ITER simulations of the TCV divertor upgrade *Plasma Physics and Controlled Fusion* **61** 085029
- [29] Wensing M, Loizu J, Reimerdes H, Duval B P, Wischmeier M and the TCV team 2020 X-point potential well formation in diverted tokamaks with unfavorable magnetic field direction *Nuclear Fusion* **60** 054005
- [30] Wensing M, Reimerdes H, Février O, Colandrea C, Martinelli L, Verhaegh K, Bagnato F, Blanchard P, Vincent B, Perek A, Gorno S, de Oliveira H, Theiler C, Duval B P, Tsui C K, Baquero-Ruiz M and Wischmeier M 2021 SOLPS-ITER validation with TCV L-mode discharges *Physics of Plasmas* **28** 082508
- [31] Smolders A, Wensing M, Carli S, De Oliveira H, Dekeyser W, Duval B P, Février O, Gahle D, Martinelli L, Reimerdes H, Theiler C, Verhaegh K and team t T C V 2020 Comparison of high density and nitrogen seeded detachment using SOLPS-ITER simulations of the tokamak á configuration variable *Plasma Physics and Controlled Fusion* **62** 125006
- [32] Senichenkov I Y, Kaveeva E G, Sytova E A, Rozhansky V A, Voskoboynikov S P, Veselova I Y, Coster D P, Bonnin X, Reimold F and the Asdex-Upgrade Team 2019 On mechanisms of impurity leakage and retention in the tokamak divertor *Plasma Physics and Controlled Fusion* **61** 045013
- [33] Wiesen S, Reiter D, Kotov V, Baelmans M, Dekeyser W, Kukushkin A S, Lisgo S W, Pitts R A, Rozhansky V, Saibene G, Veselova I and Voskoboynikov S 2015 The new SOLPS-ITER code package *Journal of Nuclear Materials* **463** 480-4
- [34] Bonnin X, Dekeyser W, Pitts R, Coster D, Voskoboynikov S and Wiesen S 2016 Presentation of the New SOLPS-ITER Code Package for Tokamak Plasma Edge Modelling *Plasma and Fusion Research* **11** 1403102-
- [35] Kaveeva E, Rozhansky V, Senichenkov I, Sytova E, Veselova I, Voskoboynikov S, Bonnin X, Pitts R A, Kukushkin A S, Wiesen S and Coster D 2020 SOLPS-ITER modelling of ITER edge plasma with drifts and currents *Nuclear Fusion* **60** 046019
- [36] Reiter D, Baelmans M and Börner P 2005 The EIRENE and B2-EIRENE Codes *Fusion Science and Technology* **47** 172-86
- [37] Bufferand H, Ciralo G, Marandet Y, Bucalossi J, Ghendrih P, Gunn J, Mellet N, Tamain P, Leybros R, Fedorczak N, Schwander F and Serre E 2015 Numerical modelling for divertor design of the WEST device with a focus on plasma-wall interactions *Nuclear Fusion* **55** 053025
- [38] Dekeyser W, Boerner P, Voskoboynikov S, Rozhansky V A, Senichenkov I, Kaveeva L, Veselova I, Vekshina E, Bonnin X, Pitts R A and Baelmans M 2021 Plasma edge simulations including realistic wall geometry with SOLPS-ITER *Nuclear Materials and Energy* **27** 100999

- [39] Senichenkov I, Kaveeva E, Rozhansky V, Shtyrkhunov N, Dolgova K, Ding R, Si H and Xu G First results of EAST edge modeling with SOLPS-ITER 3.2.0 on Extended Grid *Contributions to Plasma Physics* **n/a** e202300136
- [40] Verhaegh K, Lipschultz B, Harrison J, Duval B, Bowman C, Fil A, Gahle D S, Moulton D, Myatra O, Perek A, Theiler C and Wensing M 2021 A study of the influence of plasma–molecule interactions on particle balance during detachment *Nuclear Materials and Energy* **26** 100922
- [41] Eckstein W and Heifetz D B 1987 Data sets for hydrogen reflection and their use in neutral transport calculations *Journal of Nuclear Materials* **145-147** 332-8
- [42] Roth J and Garcia-Rosales C 1996 Analytic description of the chemical erosion of graphite by hydrogen ions *Nuclear Fusion* **36** 1647-59
- [43] Davis J W and Haasz A A 1997 Impurity release from low-Z materials under light particle bombardment *Journal of Nuclear Materials* **241-243** 37-51
- [44] Reimerdes H, Alberti S, Blanchard P, Bruzzone P, Chavan R, Coda S, Duval B P, Fasoli A, Labit B, Lipschultz B, Lunt T, Martin Y, Moret J M, Sheikh U, Sudki B, Testa D, Theiler C, Toussaint M, Uglietti D, Vianello N and Wischmeier M 2017 TCV divertor upgrade for alternative magnetic configurations *Nuclear Materials and Energy* **12** 1106-11
- [45] Guo J, Mao S, Jia G, Meng L, Li A, Xu J, Xu G and Ye M 2022 Simulation study of the influence of upstream density and power in the scrape-off layer on the double-peaked density profile at the divertor target *Nuclear Fusion* **62** 126051
- [46] Pütterich T, Fable E, Dux R, O'Mullane M, Neu R and Siccino M 2019 Determination of the tolerable impurity concentrations in a fusion reactor using a consistent set of cooling factors *Nuclear Fusion* **59** 056013
- [47] Jia G, Liu X, Xu G, Wang L, Zhu S, Xie H, Si H, Sang C, Yang Z, Xu J and Li H 2020 Simulations of Ar seeding by SOLPS-ITER for a slot-type divertor concept *Physics of Plasmas* **27** 062509
- [48] Hitzler F, Wischmeier M, Reimold F and Coster D P 2020 Impurity transport and divertor retention in Ar and N seeded SOLPS 5.0 simulations for ASDEX Upgrade *Plasma Physics and Controlled Fusion* **62** 085013
- [49] Pitcher C S, Boswell C J, Goetz J A, LaBombard B, Lipschultz B, Rice J E and Terry J L 2000 The effect of divertor baffling on Alcator C-Mod discharges *Physics of Plasmas* **7** 1894-903
- [50] Shafer M W, Covele B, Canik J M, Casali L, Guo H Y, Leonard A W, Lore J D, McLean A G, Moser A L, Stangeby P C, Taussig D, Wang H Q and Watkins J G 2019 Dependence of neutral pressure on detachment in the small angle slot divertor at DIII-D *Nuclear Materials and Energy* **19** 487-92
- [51] Reimerdes H 2023 Variable gas-baffling in the TCV divertor. In: *29th IAEA Fusion Energy Conference*, (London, United Kingdom)
- [52] Février O, Theiler C, De Oliveira H, Labit B, Fedorczak N and Baillo A 2018 Analysis of wall-embedded Langmuir probe signals in different conditions on the Tokamak à Configuration Variable *Review of Scientific Instruments* **89**
- [53] Christen N, Theiler C, Rognien T D, Rensink M E, Reimerdes H, Maurizio R and Labit B 2017 Exploring drift effects in TCV single-null plasmas with the UEDGE code *Plasma Physics and Controlled Fusion* **59** 105004
- [54] Wensing M, Reimerdes H, Février O, Colandrea C, Martinelli L, Verhaegh K, Bagnato F, Blanchard P, Vincent B, Perek A, Gorno S, de Oliveira H, Theiler C, Duval B P, Tsui C K, Baquero-Ruiz M, Wischmeier M, Team T and Team M 2021 SOLPS-ITER validation with TCV L-mode discharges *Physics of Plasmas* **28**
- [55] Niemczewski A, Hutchinson I H, LaBombard B, Lipschultz B and McCracken G M 1997 Neutral particle dynamics in the Alcator C-Mod tokamak *Nuclear Fusion* **37** 151-63
- [56] Sheikh U A, Simons L, Duval B P, Février O, Moret D, Allegrucci A, Bernert M, Crisinel F, Tersztyánszky T and Villinger O 2022 RADCAM—A radiation camera system combining foil bolometers, AXUV diodes, and filtered soft x-ray diodes *Review of Scientific Instruments* **93**
- [57] Martinelli L, Mikitchuck D, Duval B P, Andrebe Y, Blanchard P, Février O, Gorno S, Elaian H, Linehan B L, Perek A, Stollberg C, Vincent B and Team T 2022 Implementation of high-resolution spectroscopy for ion (and electron) temperature measurements of the divertor plasma in the Tokamak à configuration variable *Review of Scientific Instruments* **93**